Multi-element geochemistry across a Carlin-type gold district: Jerritt Canyon, Nevada

Lucia M. Patterson

Department of Geological Sciences and Engineering, University of Nevada, Reno (currently with Staccato Gold Resources Ltd.)

John L. Muntean*

Nevada Bureau of Mines and Geology, University of Nevada, Reno

ABSTRACT

Published district-scale maps of gold and multi-element data for districts of Carlin-type gold deposits (CTGDs) in Nevada are lacking, despite the fact that CTGDs account for 60% of annual U.S. gold production and 6.5% of annual worldwide production. In this study, maps of the hydrothermal footprint of the Jerritt Canyon district, based on distribution of gold and associated trace elements, reveal patterns that are applicable to exploration and lend insight to the nature of fluid flow in CTGDs.

The Jerritt Canyon district, located in northeastern Nevada, hosts several CTGDs, which have produced over 7 million ounces of gold. In 2000, Anglo Gold carried out multi-element analyses of the bottom 5 feet of the Roberts Mountain Formation from 6,416 drill holes scattered throughout the district. The stratigraphic interval, which occurs mainly above or within ore zones, directly overlies the Saval Discontinuity, which is paleokarst that served as a focus of subsequent deformation.

Two groups of elements were defined by gridding the data and using statistics, including correlation matrices and factor analysis. The first group consists of gold, arsenic, mercury, thallium, and tellurium, and is the elemental suite most closely associated with the CTGDs. These CTGD-related elements are commonly elevated up to several thousand feet away laterally from the vertical projection of known CTGDs at Jerritt Canyon. Decarbonatization and silicification, the two types of hydrothermal alteration most closely associated with ore, are detected by zones of low calcium, magnesium, and strontium that are centered on the deposits.

The second group of elements is characteristic of black shales and consists of two subgroups that have no apparent spatial or temporal relationship to the Carlin-type deposits. The first subgroup consists of uranium, phosphorous, lanthanum, and gallium and reflects phosphate lenses at the base of the Roberts Mountains Formation. The second group is comprised of zinc, uranium, molybdenum, vanadium, nickel, copper, cadmium, and silver, and likely represents migration of basinal brines prior to gold mineralization.

The commonly irregular distribution of ore-related hydrothermal features, in and around the CTGDs at Jerritt Canyon, suggests complex, fracture-controlled, largely vertical, hydrothermal fluid flow, rather than large-scale pervasive, lateral flow. The major center of upwelling fluids appears to be the SSX/Smith area, where gold values of ≥ 50 ppb occur in west-northwest-trending zone that is at least 25,000 feet long and 2,000 feet wide. The largest zone of elevated tellurium occurs around SSX, suggesting a possible underlying magmatic source. District-scale exploration tools derived from this study include the spatial association of CTGDs with zones of: 1) relatively pervasive, elevated gold (≥ 50 ppb), 2) strongly anomalous arsenic (≥ 50 ppm) and mercury (≥ 1 ppm), 3) elevated factor analysis scores related to CTGD-related elements, and 4) anomalous tellurium (≥ 0.2 ppm) that might indicate major upwelling zones.

*E-mail: munteanj@unr.edu

INTRODUCTION

Carlin-type gold deposits (CTGDs) of Eocene age in Nevada are epigenetic, disseminated auriferous pyrite deposits characterized by carbonate dissolution, argillization, and silicification of mainly sedimentary rocks (Hofstra and Cline, 2000; Cline *et al.* 2005). CTGDs in Nevada dominate gold (Au) production in the United States and constitute 6.5% of annual world production, making the United States one of the leading gold-producing countries in the world (NBMG, 2009). To date, exploration for CTGDs has focused on recognition of favorable stratigraphy (e.g., calcareous lithologies), structure (e.g., lower plates of thrust faults, high-angle faults, structural culminations), hydrothermal alteration (e.g., jasperoid, decarbonatization), and Au assays. In addition, pathfinder elements associated with CTGDs, including arsenic (As), mercury (Hg), and antimony (Sb), have also led to the discovery of many CTGDs such as at Cortez (Wells *et al.*, 1969), Jerritt Canyon (Birak and Hawkins, 1985) and Goldstrike (Bettles, 2002). Though these tools have been successful in the discovery of many CTGDs, especially those exposed at the surface, most deposits in the future will likely have to be discovered underneath cover, including pre-ore bedrock and post-ore bedrock or alluvium. Additional exploration tools and improved genetic models for CTGDs are necessary to improve the efficiency in exploring for these blind deposits.

Understanding the extent of the hydrothermal system and the patterns of geochemistry and hydrothermal alteration within the system of a targeted deposit type is critical in exploration under cover. Knowing the extent of the system increases the target size, and knowing the patterns within the system helps in vectoring toward ore, either laterally or vertically. For example, zoning patterns in alteration and trace elements are widely used in exploration of other deposit types, such as porphyry and epithermal deposits, but have not been as successfully applied to the exploration of CTGDs.

Published studies have documented alteration and geochemical patterns within and outboard of individual CTGDs. Vertical and lateral zoning patterns between Au and associated trace elements at the Deep Star deposit have been documented most recently by Heitt *et al.* (2003). Correlations between Au and clay minerals in CTGDs have been documented by Kuehn and Rose (1992) at the Carlin deposit, Cail and Cline (2001) at the Getchell deposit, and Heitt *et al.* (2003) at Deep Star. Depletion halos in the $\delta^{18}O$ values of carbonate around known CTGDs were demonstrated by Stenger *et al.* (1998) at the Twin Creeks deposit, and Arehart and Donelick (2006) at the Pipeline deposit. Large zones of reset apatite fission-tracks dates surrounding CTGDs at the district scale occur in the Carlin trend (Chakurian *et al.*, 2003; Cline *et al.*, 2005), and at Pipeline (Arehart and Donelick, 2006). Though these studies are critical

to understanding the hydrothermal footprint of CTGDs, most have been done at the scale of individual deposits and not at the district-scale.

The Jerritt Canyon district in northeastern Nevada contains several CTGDs within an area of over 250 square kilometers (Figure 1). The total Au endowment of the district is nearly 10 million ounces (Jones, 2005). In 2000, Anglo Gold Corporation, then the operator of the Jerritt Canyon mine, collected a dataset consisting of 6,416 multi-element geochemical analyses of the base of the Roberts Mountains Formation, directly above the Saval discontinuity. The analyses were of drill core or cuttings from 5-foot intervals from holes drilled throughout the district. The Saval discontinuity marks the contact with the underlying Hanson Creek Formation (Figure 2). Rocks along the Saval discontinuity are commonly altered and anomalous in trace elements, suggesting that it once served as an aquifer and played a key role with respect to fluid flow. The lithology at the base of the Roberts Formation in almost every drill hole is calcareous siltstone. Thus, the data set eliminates the effect of variable lithologies, allowing for a more defined picture of the hydrothermal footprint of the CTGDs at Jerritt Canyon. Furthermore, unlike many other districts of CTGDs, Jerritt Canyon does not have any known Mesozoic intrusions and associated hydrothermal alteration and mineralization, which would interfere with the later hydrothermal alteration and geochemical signature associated with Carlin-type mineralization.

This paper focuses on the multi-element analyses along the Saval. First, statistical techniques are employed to establish which elements are associated with Au and to resolve other distinct groups of elements. Then, the spatial distributions of Au and related trace elements, of elements associated with CTGD-related alteration, and of other elements not associated with Au mineralization are presented as series of maps of gridded values at the district scale. From these maps, conclusions are drawn on the extent of the geochemical halos around CTGDs at Jerritt Canyon and their bearing on exploration and hydrothermal fluid flow.

DISTRICT HISTORY AND GEOLOGY

History

The Jerritt Canyon district is located 45 miles north of Elko, in the Independence Mountains. Historic exploration activity in the district was concentrated on Sb with minimal production during the early 1900's. The discovery of Au mineralization in the district was preceded by an Sb exploration program initiated by FMC Inc. in 1971 (Birak and Hawkins, 1985). The initial gold discovery in the district was made in 1973 when geologists
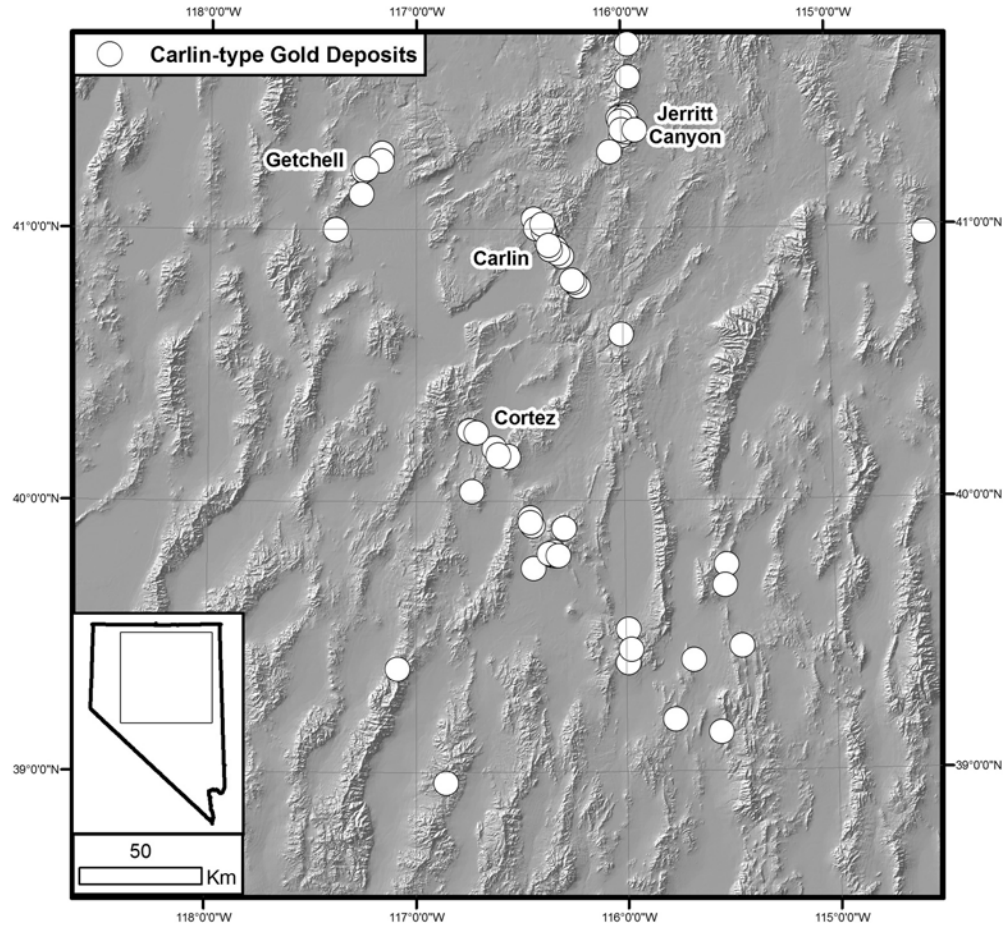
Figure 1. Digital elevation model of northern Nevada, showing locations of CTGDs and the locations of the four large clusters of large CTGDs, including Jerritt Canyon.

recognized similarities between the geology of Jerritt Canyon and the nearby Carlin Au deposit. Mapping, sampling, and geochemical analyses led to the discovery of a Au anomaly along the north fork of Jerritt Creek. A joint-venture agreement between Freeport Exploration Company and FMC in 1976 led to an expanded mapping, sampling and drilling program that resulted in the delineation of several deposits and commencement of production in 1981 (Birak and Hawkins, 1985). Several companies have managed the Jerritt Canyon mine since Freeport, including Independence Mining Company (1990–1999), Anglo Gold (1999–2003), Queenstake Resources (2003–2007), and currently Yukon-Nevada Gold Corporation. To date, Jerritt Canyon has produced over seven million ounces of Au. Until recently, annual production had been mainly between 170,000 ounces and 350,000 ounces of Au. Proven and probable reserves at the end of 2009 stood at 3.1552 million tons, grading 0.227 opt Au.

Geology

The geology of the Jerritt Canyon district has been presented in several publications (i.e., Kerr, 1962; Birak and Hawkins, 1985; Daly *et al.*, 1991; Hofstra, 1994; Peters *et al.*, 2003; Eliason and Wilton, 2005; Muntean and Henry, 2007). A stratigraphic column and a geologic map of the north half of the Jerritt Canyon district are shown in Figures 2 and 3, respectively. Paleozoic stratigraphy is characterized by eugeosynclinal (upper plate) rocks that have been thrust eastward over the miogeosynclinal (lower plate) rocks along the Roberts Mountains Thrust during the late Devonian to early Mississippian Antler orogeny.

The oldest lower plate rocks exposed in the Jerritt Canyon district are limestone of the Ordovician Pogonip Group, which is overlain by the Ordovician Eureka Quartzite. Overlying the Eureka Quartzite is the main host rock in the district, which is the Silurian to Ordovician Hanson Creek Formation (SOhc). It has a maximum thickness of about 750 feet and is divided informally into five units. The lowermost unit, Unit 5 ($SOhc_5$), consists of chert, limestone, and laminated calcareous siltstones. Unit 4 ($SOhc_4$) is a carbonaceous, medium to coarse-grained limestone, commonly with lenses of black chert. Unit 3 ($SOhc_3$), which hosts much of the ore in the district, consists of interbedded carbonaceous micritic limestone and argillaceous dolomitic limestone. Unit 2 ($SOhc_2$) is a light gray limestone, up
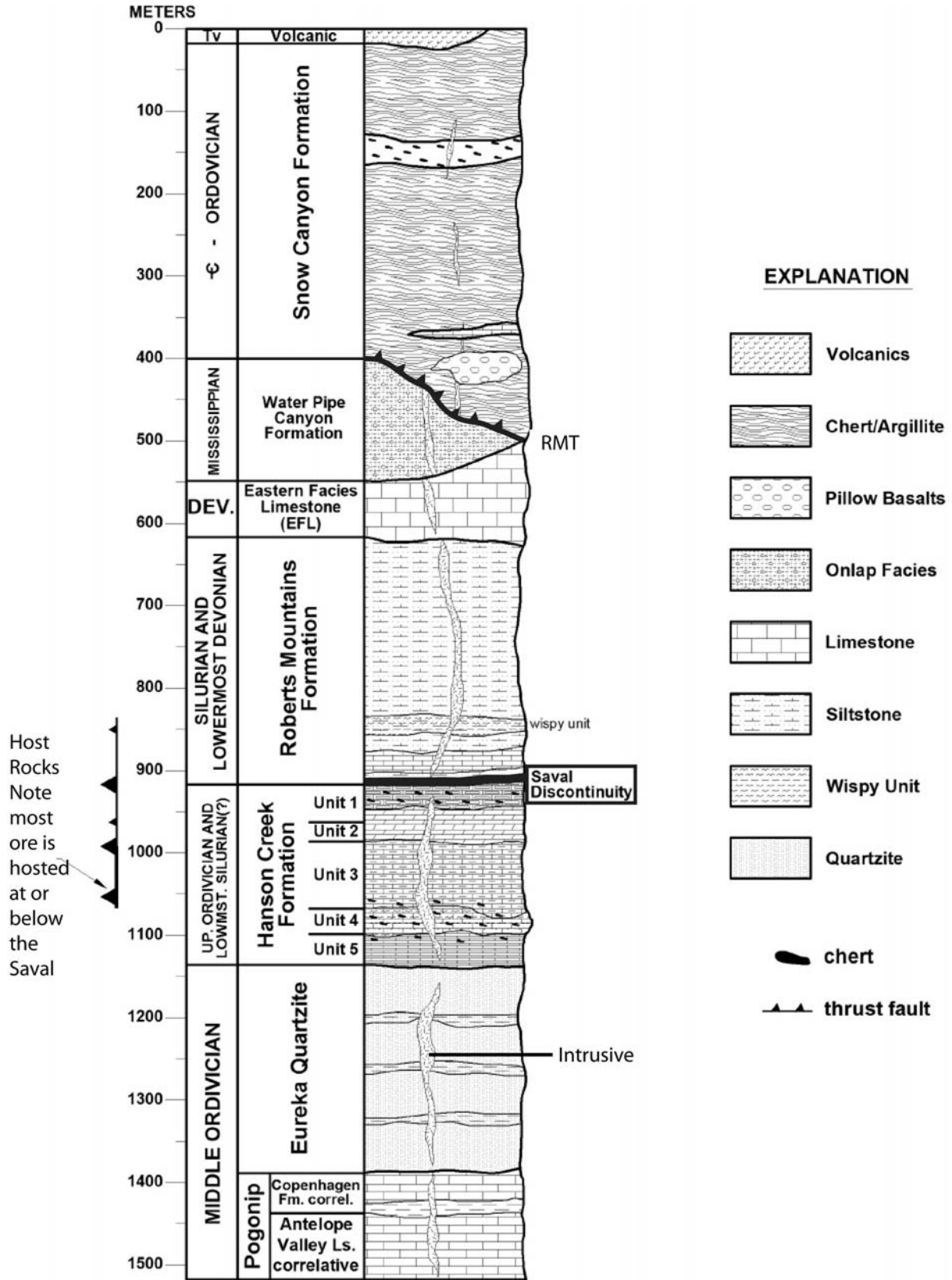
Figure 2. Jerritt Canyon stratigraphic section. The lower contact of the Roberts Mountains Formation, labeled "Saval Discontinuity" marks the location of the sample interval for Anglo Gold data set. "RMT" marks the location of the Roberts Mountains thrust fault that is discussed in the text. Modified from Eliason and Wilton (2005).
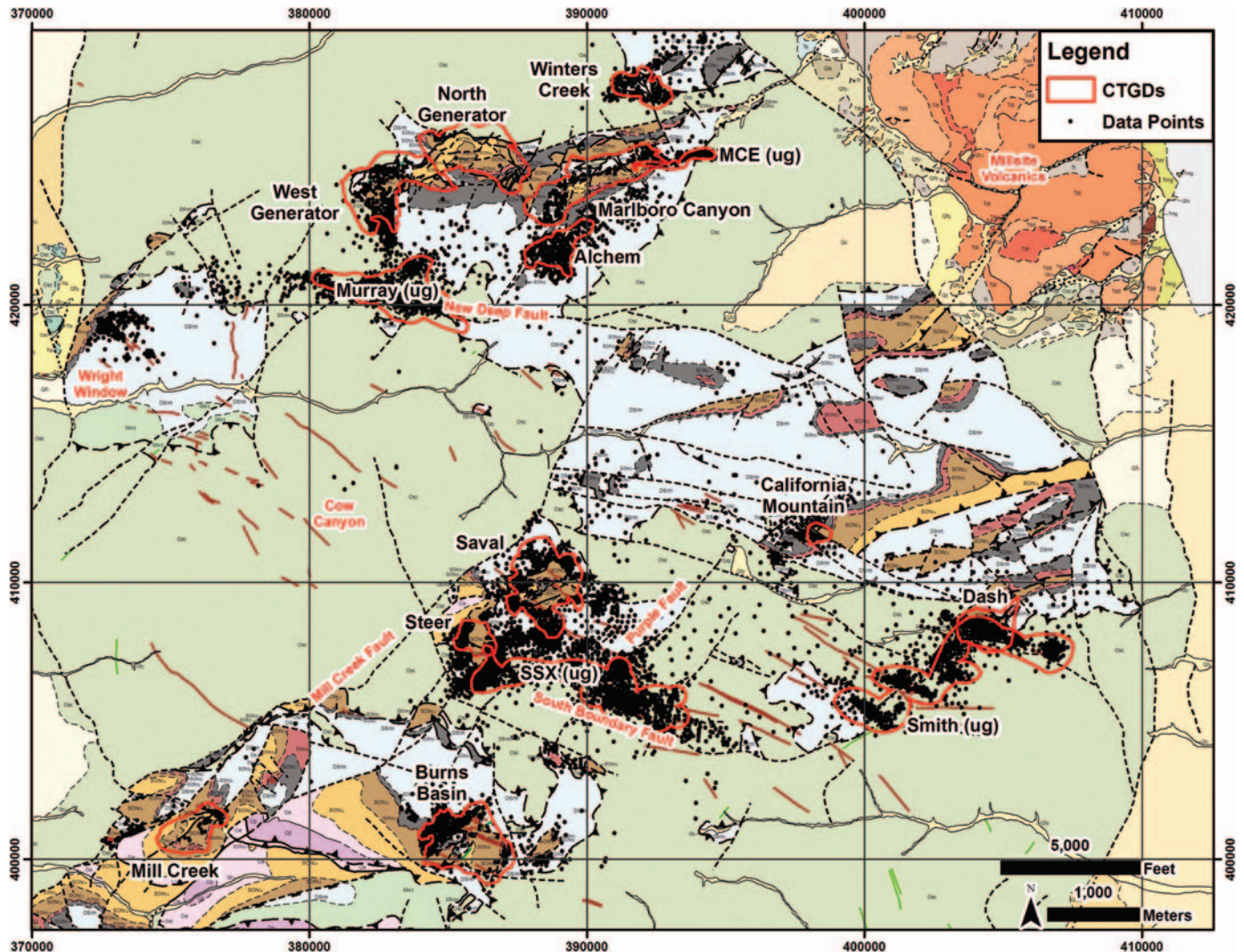
Figure 3. Geologic map of the Jerritt Canyon district taken from Muntean and Henry (2007), showing locations of Carlin-type gold deposits (CTGDs, red outlines, black text), surface projection of the Saval data points (black dots) and specific features discussed in the text (red text). In general, the light blue is the Roberts Mountains Formation (DSrm), the areas of gray-maroon-brown-yellow are respectively units 1–4 of the Hanson Creek Formation (SOhc). The contact between the DSrm (light blue) and unit 1 of the SOhc marks the Saval discontinuity, though it can occur between the DSrm and lower units of the SOhc. Basal unit 5 of the SOhc, which has been recognized in drilling but has not been mapped consistently in the past, has been combined with unit 4. Light and dark purple are Eureka Quartzite (Oe) and Pogonip Group (Op), respectively. Areas of green and blue-gray are upper plate siliciclastic, chert and greenstone of the Snow Canyon Formation and McAfee Quartzite, respectively (Osc and Om). Orange is Tertiary volcanic rocks, and yellow-tan Quaternary sediments. The maroon lines generally trending west-northwest are mostly Pennsylvanian dikes. The thick black lines (commonly dashed) are faults. A complete legend can be found in Muntean and Henry (2007). Coordinates are longitude-latitude (tics, degrees-minutes, WGS84) and local Jerritt Canyon mine grid (grid lines, feet, NAD27 Nevada West State Plane modified by a false northing of -2,000,000 ft).

to 100 feet thick, and is commonly fossiliferous and dolomitized. Unit 1 ($SOhc_1$) is the uppermost unit of the Hanson Creek Formation and is a 10 to 130 foot-thick sequence of rhythmically interbedded black chert and carbonaceous limestone. The Roberts Mountains Formation (DSrm), of Silurian to Devonian age, unconformably overlies the SOhc along the Saval discontinuity as mentioned above. It is predominantly a laminated, calcareous to dolomitic, carbonaceous siltstone. The lower parts of the DSrm host significant ore in the district. Locally, the Roberts Mountains Formation is unconformably overlain by a Mississippian foredeep sequence called the Water Pipe Canyon Formation, which consists of greywacke, carbonaceous shale, chert-pebble conglomerate, and bedded chert.

Upper plate rocks in the Jerritt Canyon district include the Snow Canyon Formation and McAfee Quartzite. The Snow Canyon Formation consists of chert, argillite, siltstone, shale, turbiditic quartzite, limestone, and greenstone (metabasalt), whereas the McAfee Quartzite is a massive clean quartzite with minor shale and chert. Based on published age data, the formations are considered to be late Cambrian to Ordovician in age. However, ongoing biostratigraphic work has demonstrated ages as young as upper Devonian (P. Noble, personal

communication, 2007; C, Holm-Denoma, personal communication, 2009).

The structural geology of the Jerritt Canyon district is characterized by multiple episodes of thrusting, folding, and high-angle faulting. Lower plate stratigraphy is commonly imbricated and locally interleaved with thin slices of upper plate rocks. High-angle faults also have complicated histories and show evidence for normal, strike-slip and reverse movement. In addition to the Antler Orogeny, the geology of the Independence Mountains and other nearby ranges strongly suggests the Jerritt Canyon district should have also experienced deformation from the Sonoma, Nevadan, and Sevier Orogenies. For example, just north of Figure 3, rocks of the Golconda allochthon are thrust over a Mississippian to Permian overlap sequence that overlies the Roberts Mountain allochthon and lower plate rocks. East of the Independence Mountains, the Adobe syncline is thought to have formed in the hinterland of the Sevier Orogeny. However, 321 Ma basalt/andesite dikes, which mainly occupy steeply dipping, west-northwest-striking faults, cross-cut thrust faults, folds, and all lower and upper plate units and show little evidence of subsequent deformation, suggesting most of the folding and thrusting in the Jerrritt Canyon district is Mississippian or older, and possibly entirely related to the Antler Orogeny (Phinisey *et al.*, 1996; Hofstra *et al.*, 1999).

In addition to the late Mississippian basalt/andesite dikes, there are basalt and quartz monzonite dikes of Eocene age (Phinisey *et al.*, 1996; Hofstra *et al.*, 1999). The Eocene dikes strike northeast and are locally altered and mineralized. Eocene sedimentary and volcanic rocks unconformably overlie the Paleozoic rocks along the flanks of the range on the northeast, southeast, and southwest sides of the Jerritt Canyon district. Lithologies include a basal conglomerate, lacustrine limestone and shale, various rhyolite ash flow tuffs, and dacite lavas and tuffs that occur mainly in the area known locally as the Millsite Volcanics on the northeastern end of the district (Figure 3; Henry, 2008). These Eocene sedimentary and volcanic rocks are nowhere mineralized. In addition, unaltered Miocene basalt dikes locally occur (Eliason and Wilton, 2005).

Post-ore structures are mainly related to basin and range extension. In general, basin and range faults trend north-south and displace ore bodies, dikes, and volcanic rocks. The range-front faults flanking the Independence Mountains are the largest extensional structures in the district.

Ore Bodies

Gold mineralization at Jerritt Canyon has been described by many workers (Birak and Hawkins, 1985; Daly *et al.*, 1991; Bratland, 1991; Hofstra, 1994; Dewitt, 1999; Hofstra *et al.*, 1999; Hutcherson, 2002; Eliason and Wilton, 2005; McMillin, 2005). Gold deposits were first found in lower plate windows, where ore bodies are hosted mainly by the Hanson Creek and Roberts Mountains Formations, and in the late Mississippian basalt/andesite dikes (Figures 2 and 3). Since 1991, deposits have been found in lower plate rocks covered by upper plate rocks. The deposits tend to be tabular in morphology, but are commonly highly irregular. Deposit geometry is controlled by intersections of favorable lithologies with a complex array of structures. Ore bodies occupy many pre-Tertiary high- and low-angle structures, both extensional and compressional. They are also found in imbricated sections. The highest grades and largest deposits occur where west-northwest-trending high-angle faults, dikes, and fold structures intersect northeast-striking, high-angle faults in combination with favorable lithologies. In most cases the ore is refractory (due to carbon and pyrite), although oxidized supergene ore zones were present in the Alchem, California Mountain, and Marlboro Canyon deposits. The high-grade refractory ores in the district commonly occur in decarbonatized, silicified, and sulfidized rocks, and locally contain orpiment and realgar. The gold in refractory ores is mainly contained in arsenian pyrite and marcasite. The age of the gold deposits is constrained between 40.8 Ma and 17.8 Ma, which are the ages of the locally mineralized Eocene basalt dikes and the unmineralized Miocene dikes, respectively (Hofstra *et al.*, 1999; Eliason and Wilton, 2005).

Saval Discontinuity

As described above, the Saval discontinuity marks the contact between the DSrm and underlying SOhc (Figure 2). Missing sections of SOhc are common below the Saval. The DSrm is commonly found in direct contact with $SOhc_2$, $SOhc_3$, or $SOhc_4$. The Saval discontinuity has been interpreted as a low-angle structural feature (Bratland, 1991; Eliason and Wilton, 2005), a tectonically activated disconformity (Daly *et al.*, 1991), and an erosional karsted disconformity (Peters *et al.*, 2003). Patterson (2009), based on field mapping of surface exposures in five localities, logging of several hundred drill holes, and petrography, concluded that the discontinuity was originally an unconformity formed during subaerial exposure, erosion, and karstification that occurred during a lowstand in sea level during the early Silurian. The unconformity subsequently served as a focus of later deformation caused by a rheologic contrast between the more competent SOhc (especially the $SOhc_2$ and $SOhc_1$) and the overlying DSrm. The more shaly DSrm took up most of the strain along the Saval.

Rocks along the Saval are commonly altered and anomalous in trace elements, suggesting it once served as a paleo-aquifer. Silicification of the $SOhc_1$ underneath the Saval is very common. Hofstra (1994) identified 17 stages of quartz in the jasperiod of the $SOhc_1$ and summarized them into three silicification events: 1) pre-ore, 2) ore-stage, and 3) late-ore stage.

It is important to note that the Saval only locally constitutes ore. It mostly occurs distal to ore. As pointed out above, the dominant ore host at Jerritt Canyon is $SOhc_3$; therefore, in many cases, the Saval occurs above ore zones. The locations of the CTGDs at Jerritt Canyon are shown in Figure 3 and their relative positions with respect to the Saval are summarized in Table 1. In

Table 1. POSITION OF GOLD DEPOSITS AT JERRIT CANYON RELATIVE TO THE SAVAL DISCONTINUITY.

Deposit	Predominant Host Unit(s)	Predominant Position Relative to the Saval
Alchem	DSrm	40–200 ft above
Winters Creek	DSrm	25–160 ft above
West Generator	DSrm, SOhc$_3$	straddles
Murray	SOhc$_3$, DSrm	straddles
Marlboro Canyon	SOhc$_3$, DSrm	straddles
Burns Basin	SOhc$_3$, DSrm	straddles
Smith	SOhc$_3$, SOhc$_2$	0–100 ft below
Steer	SOhc$_3$	0–100 ft below
California Mountain	SOhc$_3$	0–100 ft below
Dash	SOhc$_3$, SOhc$_2$	0–150 ft below
North Generator	SOhc$_3$	0–250 ft below
Saval	SOhc$_3$	0–250 ft below
SSX	SOhc$_3$	0–375 ft below
Mill Creek	SOhc$_3$	80–250 ft below

the SSX, Smith, North Generator, Dash, Saval, Steer, California Mountain, and Mill Creek deposits, ore is primarily occurs in SOhc$_3$, up to 375 feet below the Saval. The Murray, West Generator, Marlboro Canyon, and Burns Basin deposits straddle the Saval. The Saval is located up to 200 feet below the Alchem and Winters Creek deposits. It is also important to reiterate that these deposits are not stratabound. They are strongly controlled by structure; therefore, areas of mineralization are commonly found transecting units of the SOhc and extending up into the DSrm. Below, the geochemistry along the Saval is displayed as two-dimensional maps, and the geochemical halos to the deposits are addressed with respect to the vertical projection of the deposits.

DESCRIPTION OF THE DATASET

As stated above, in 2000 Anglo Gold analyzed 6,416 drill samples (core and chips) for multi-element geochemistry of the bottom 5 feet of the Roberts Mountains Formation directly above the Saval discontinuity. In drill holes with imbricated sections, the samples were taken from the five foot interval directly above the first downhole occurrence of the Saval. Because of imbrication, not all the samples may be time-equivalent. Attempts were made to separate conodonts from seven samples, to determine whether or not samples were time-equivalent. Unfortunately, no conodonts were recovered.

Figure 3 shows the distribution of the samples projected to the surface. The elevations of the samples are mostly between 6,000 and 7,500 feet. Figure 3 is a subset of the dataset, showing only samples in the north half of the Jerrit Canyon district, where all past production has occurred. Only about 300 samples occur south of Figure 3. The relatively wide spacing of these 300 samples prevented reliable gridding and interpretation; thus, only the samples in the north half of the district are presented in this paper. Sample spacing is irregular with the greatest density being, understandably, around the deposits. How-

ever, the relative lack of data in the vicinity of the Marlboro Canyon and North Generator deposits, reflects erosion of the Saval discontinuity prior to mining of those deposits. Figure 3 shows a natural division of the sample set into 2 halves. For the remainder of the paper, the north half is referred to as the Murray/Winters Creek area, and the south half is referred to as the SSX/Smith area.

All analyses were completed by ALS Chemex. Au was determined by fire assay with an AA finish, while other elements were analyzed by ICP-MS-AES, using a nitric acid-aqua regia digestion. Elements not completely digested by nitric acid-aqua regia include Al, Ba, Be, Ca, Cr, Ga, K, La, Mg, Na, Sr, Ti, and W, especially if they are in silicates or refractory minerals such as Fe-Ti oxides, chromite, scheelite and barite. If a given element was not detected in a sample, a value of half the detection limit of that given element was entered into the database that was used for statistical analysis, gridding, and plotting in GIS. Ti, Ge, and B were not included in the interpretation of the data, because very few samples had values exceeding the detection limits for those three elements.

STATISTICS

To help define elemental associations within the data set, a variety of statistical analyses were undertaken. Table 2 shows standard descriptive statistics for each element. In addition, Spearman rank correlation matrices, traditional R-mode factor analysis, and correspondence analysis were completed.

Estimated Background

Given the sampling was biased toward Au mineralization, we used a somewhat arbitrary approach to estimate background concentrations, which assumed to represent trace element concentrations prior to Au mineralization in the Eocene. In order to establish background, samples were chosen from the dataset that had low Au, Tl, Hg, As, Te, and Sb, which is the elemental suite associated with Au mineralization as outlined below. Analyses were considered low if Au values were <5ppb (the detection limit for Au) and also had <0.25 ppm Tl, <2ppm Hg, <10ppm As, <0.15 ppm Te, and <13ppm Sb. These are arbitrary thresholds. Seventy-nine samples met those criteria, and the calculated means for all the elements for those samples are shown in the last column in Table 2. These values are our best estimate of local background concentrations prior to Carlin-type gold mineralization in the Eocene (Table 1). The complete analyses of all 79 samples can be found in Patterson (2009).

Correlation Matrices

Spearman rank correlation matrices were completed using the statistical software package SYSTAT 11. The Spearman rank correlation coefficients were utilized because they do not rely on a linear correlation between two variables as does the

Table 2. DESCRIPTIVE STATISTICS, DETECTION LIMITS, AND ESTIMATED BACKGROUND VALUES.

Element	Minimum	Maximum	Range	Median	Mean	Standard Deviation	Skewness	Detection Limit	Upper Limit	Estimated Background
Au (ppb)	2.5	82859	82856.5	125	732.74	2783.24	13.50	5	686,000	2.50
Ag (ppm)	0.01	26.7	26.69	0.35	0.58	1.12	10.29	0.02	100.0	0.21
Al (%)	0.01	6.50	6.49	0.30	0.36	0.69	67.16	0.01	15.00	0.29
As (ppm)	0.1	10,000.0	9,999.9	71.4	178.96	571.40	11.91	0.2	10,000	5.37
Ba (ppm)	5	4,270	4,265	240	586.65	827.23	2.19	10	10,000	258.01
Be (ppm)	0.025	6.25	6.225	0.40	0.44	0.28	3.93	0.05	100	0.35
Bi (ppm)	0.005	5.00	4.995	0.06	0.08	0.13	22.93	0.01	10,000	0.05
Ca (%)	0.04	15.00	14.96	7.38	7.17	4.16	0.12	0.01	15.00	12.53
Cd (ppm)	0.01	115.50	115.49	0.98	1.74	3.78	13.62	0.02	500	0.87
Co (ppm)	0.1	92.6	92.5	3.2	3.88	3.83	8.11	0.2	10,000	3.33
Cr (ppm)	0.5	734	733.5	48	71.08	68.55	2.53	1	10,000	29.58
Cu (ppm)	0.1	1,515.0	1,514.9	19.0	22.48	27.26	34.08	0.2	10,000	14.17
Fe (%)	0.03	11.30	11.27	0.94	1.04	0.58	4.91	0.01	15.00	0.72
Ga (ppm)	0.05	16.0	15.95	1.0	1.20	0.91	4.34	0.1	10,000	0.80
Hg (ppm)	0.005	4,370.00	4,369.995	2.69	6.89	57.01	70.36	0.01	10,000	0.31
K (%)	0.01	3.00	2.99	0.14	0.16	0.09	6.43	0.01	10.00	0.13
La (ppm)	5	450	445	5	8.21	10.41	17.10	10	10,000	8.63
Mg (ppm)	0.01	10.40	10.39	3.21	3.12	2.89	19.41	0.01	15.00	3.96
Mn (ppm)	2.5	4,990	4,987.5	120	143.94	130.56	11.38	5	10,000	154.56
Mo (ppm)	0.1	184.0	183.9	5.2	7.45	8.40	5.61	0.2	10,000	5.34
Na (%)	0.01	0.13	0.12	0.01	0.03	0.01	8.31	0.01	10.00	0.01
Ni (ppm)	0.5	2,030	2,029.5	24	28.43	36.90	38.72	1	10,000	18.52
P (ppm)	10	10,000	9,990	1,600	2,270.80	2,179.75	2.01	10	10,000	1545.70
Pb (ppm)	1	802	801	7	9.59	18.69	20.83	2	10,000	5.46
Sb (ppm)	0.1	10,000.0	9,999.9	13.3	81.64	456.67	15.44	0.1	10,000	2.58
Sc (ppm)	0.5	27	26.5	2	2.29	1.66	3.77	1	10,000	1.76
Se (ppm)	0.10	50.20	50.10	1.50	2.21	2.75	4.85	0.50	1,000	1.52
Sr (ppm)	0.5	1,925	1,924.5	70	96.57	129.41	6.59	1	10,000	362.89
S (%)	0.005	5.00	4.995	0.30	0.46	0.53	2.76	0.01	5.00	0.45
Te (ppm)	0.01	26.40	26.39	0.05	0.22	1.01	14.79	0.02	500.00	0.04
Tl (ppm)	0.01	160.00	159.99	0.48	1.64	6.33	13.21	0.02	10,000	0.08
W (ppm)	0.025	762.00	761.975	0.85	1.53	11.00	56.77	0.05	10,000	0.26
U (ppm)	0.025	131.50	131.475	2.55	4.23	6.59	8.16	0.05	10,000	3.96
V (ppm)	0.5	3,120	3,119.5	39	57.03	111.42	13.45	1	10,000	32.27
Zn (ppm)	1	9,900	9,899	112	169.38	364.86	18.98	2	10,000	77.75

more traditional Pearson correlation coefficient, which can be strongly influenced by outliers. A Spearman rank correlation coefficient of 1 is produced when two variables being compared are monotonically related. For example, if all the samples were intentionally listed in order of increasing Au and, upon inspection, all the corresponding As values were also in order of increasing values, Au and As would have Spearman correlation coefficient of 1, even if Au and As do not form a linear trend when plotted on a graph.

The Spearman correlation matrix for selected elements, including the corresponding scatterplots, is shown in Figure 4. Gold correlates strongly with Hg (0.65), As (0.56), and Tl (0.55), and less so with Te (0.40), Ag (0.33), Sb (0.28) and S (0.22). Gold negatively correlates with Ca (−0.28), Sr (−0.28), and Mg (−0.16). Examples of other strong positive correlations include K:Al (0.91), Ca:Sr (0.83), Ca:Mg (0.76), Hg:Tl (0.69), U:P (0.68), U:Mo (0.66), Tl:As (0.63), Ni:Zn (0.63), Ni:Cu (0.62), Ni:V (0.62), Ni:Bi (0.62), Co:Fe (0.61), Cu:Fe (0.61), As:Hg (0.60), U:V (0.59), P:V (0.57), and Zn:V (0.55). Exam-

ples of other strong negative correlations include Sb:Mg (−0.54), Sb:Ca (−0.49), and Sb:Sr (−0.41). Spearman rank correlation matrices were also completed on the following subsets of the dataset: 1) samples within the vertical projections of known Au deposits, and 2) samples outside the vertical projections of known Au deposits. However, they showed nothing notably different than the entire dataset. All of the correlation matrices showing all of the elements are in Patterson (2009).

Factor Analysis

Factor analysis for the entire dataset was completed using SYSTAT 11. Traditional R-mode factor analysis was utilized, using varimax rotation and a minimum eigen value of 1.00. Varimax rotation was used because it maximizes the variance that each factor represents (Abdi, 2003). Most of the elements have approximate log-normal distributions; therefore, the analyses were converted to logarithms prior to calculations, because factor analysis is based on the assumption of normal popula-
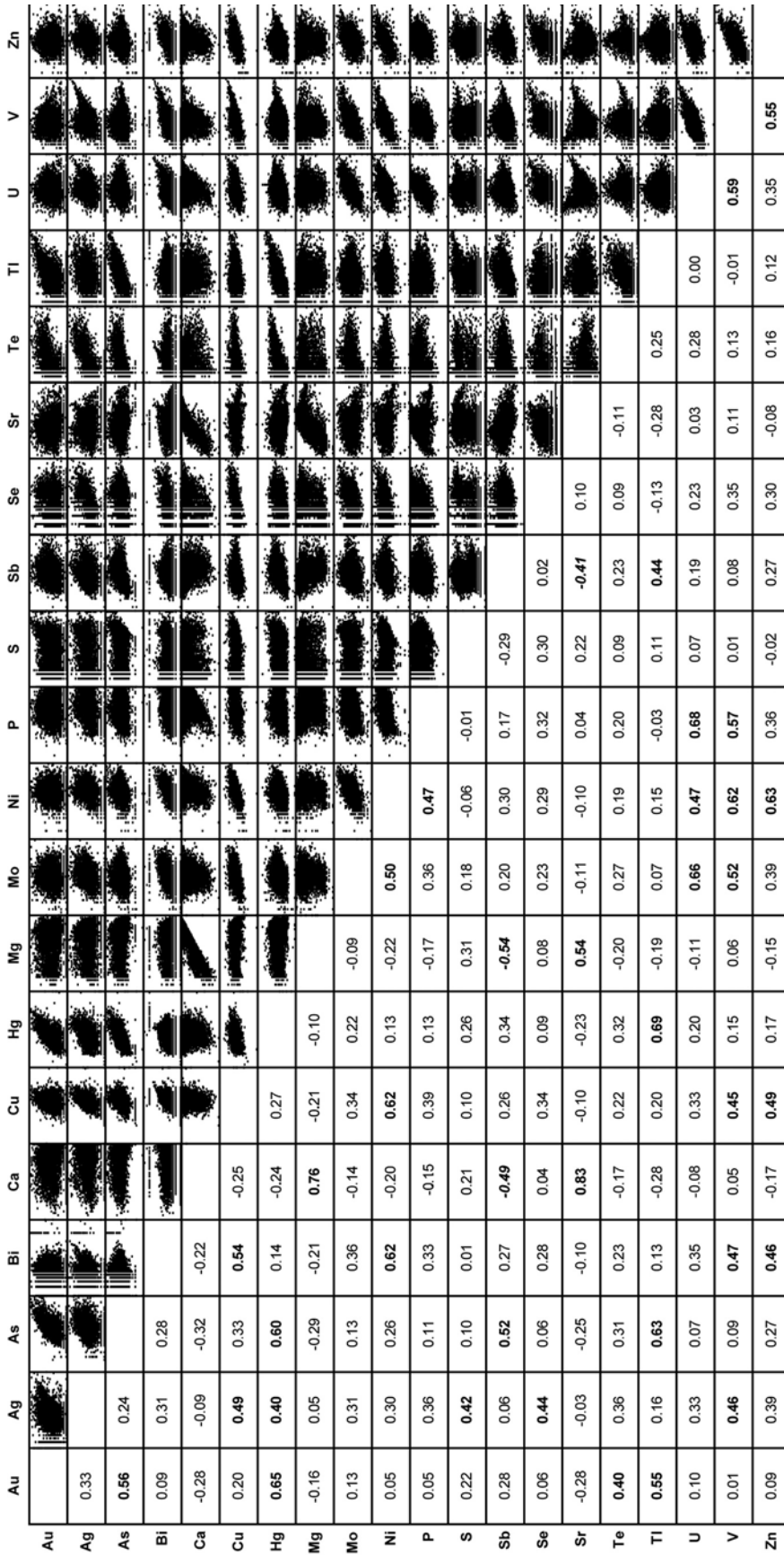
	Au	Ag	As	Bi	Ca	Cu	Hg	Mg	Mo	Ni	P	S	Sb	Se	Sr	Te	Tl	U	V	Zn
Ag	0.33																			
As	**0.56**	0.24																		
Bi	0.09	0.31	0.28																	
Ca	-0.28	-0.09	-0.32	-0.22																
Cu	0.20	**0.49**	0.33	**0.54**	-0.25															
Hg	**0.65**	**0.40**	**0.60**	0.14	-0.24	0.27														
Mg	-0.16	0.05	-0.29	-0.21	**0.76**	-0.21	-0.10													
Mo	0.13	0.31	0.13	0.36	-0.14	0.34	0.22	-0.09												
Ni	0.05	0.30	0.26	**0.62**	-0.20	**0.62**	0.13	-0.22	**0.50**											
P	0.05	0.36	0.11	0.33	-0.15	0.39	0.13	-0.17	0.36	**0.47**										
S	0.22	**0.42**	0.10	0.01	0.21	0.10	0.26	0.31	0.18	-0.06	-0.01									
Sb	0.28	0.06	**0.52**	0.27	***-0.49***	0.26	0.34	***-0.54***	0.20	0.30	0.17	-0.29								
Se	0.06	**0.44**	0.06	0.28	0.04	0.34	0.09	0.08	0.23	0.29	0.32	0.30	0.02							
Sr	-0.28	-0.03	-0.25	-0.10	**0.83**	-0.10	-0.23	**0.54**	-0.11	-0.10	0.04	0.22	***-0.41***	0.10						
Te	**0.40**	0.36	0.31	0.23	-0.17	0.22	0.32	-0.20	0.27	0.19	0.20	0.09	0.23	0.09	-0.11					
Tl	**0.55**	0.16	**0.63**	0.13	-0.28	0.20	**0.69**	-0.19	0.07	0.15	-0.03	0.11	**0.44**	-0.13	-0.28	0.25				
U	0.10	0.33	0.07	0.35	-0.08	0.33	0.20	-0.11	**0.66**	**0.47**	**0.68**	0.07	0.19	0.23	0.03	0.28	0.00			
V	0.01	**0.46**	0.09	**0.47**	0.05	**0.45**	0.15	0.06	**0.52**	**0.62**	**0.57**	0.01	0.08	0.35	0.11	0.13	-0.01	**0.59**		
Zn	0.09	0.39	0.27	**0.46**	-0.17	**0.49**	0.17	-0.15	0.39	**0.63**	0.36	-0.02	0.27	0.30	-0.08	0.16	0.12	0.35	**0.55**	

Figure 4. Correlation matrix of 20 selected trace elements based on the 6,416 analyses in the Saval dataset. Shows Spearman rank correlation coefficients and accompanying scatter plots. Correlation coefficients ≥0.4 are in bold typeface, and those ≤0.4 are in bold italics. Correlation matrices for all the elements can be found in Patterson (2009).

Table 3. **LOADINGS FOR FIVE STRONGEST FACTORS IDENTIFIED IN FACTOR ANALYSIS.**

Element	Factor 1	Factor 2	Factor 3	Factor 4	Factor 5
Au	−0.031	0.115	**0.787**	0.046	0.006
Ag	0.110	0.055	0.353	**0.628**	0.256
Al	0.282	0.023	0.061	0.097	**0.870**
As	−0.019	0.128	**0.766**	0.019	0.302
Ba	−0.056	−0.019	0.021	0.134	−0.004
Be	0.089	−0.313	−0.010	0.189	**0.695**
Bi	0.149	0.138	0.102	0.296	**0.614**
Ca	0.113	*−0.930*	−0.142	0.016	−0.019
Cd	0.077	−0.083	0.098	**0.828**	0.243
Co	−0.137	−0.171	0.102	0.167	**0.621**
Cr	0.376	**0.514**	0.186	0.294	−0.126
Cu	0.100	0.122	0.225	**0.464**	**0.559**
Fe	−0.195	0.053	0.312	0.162	**0.718**
Ga	**0.425**	0.128	0.138	0.217	**0.750**
Hg	0.068	0.035	**0.848**	0.150	0.089
K	0.182	−0.126	0.088	0.070	**0.869**
La	**0.721**	−0.095	−0.145	0.066	0.367
Mg	−0.074	*−0.863*	−0.083	0.095	−0.003
Mn	−0.262	*−0.751*	0.053	0.040	0.212
Mo	0.322	0.067	0.132	**0.675**	0.002
Na	0.008	−0.048	−0.001	0.048	0.091
Ni	0.217	0.097	0.059	**0.520**	**0.526**
P	**0.765**	0.077	0.048	0.301	0.280
Pb	0.120	0.173	−0.043	0.231	0.312
S	−0.121	−0.375	0.254	0.181	0.040
Sb	0.112	**0.470**	**0.416**	0.076	0.071
Sc	−0.032	−0.263	−0.012	0.112	**0.680**
Se	0.094	−0.009	−0.116	**0.433**	0.281
Sr	0.220	*−0.785*	−0.181	−0.143	0.083
Te	0.127	0.123	**0.580**	0.189	−0.039
Tl	−0.117	0.037	**0.829**	−0.055	0.128
U	**0.739**	0.054	0.091	**0.498**	0.027
V	**0.423**	−0.030	−0.039	**0.663**	0.389
W	0.301	0.293	0.374	0.152	0.016
Zn	0.073	0.031	0.076	**0.737**	0.333
% Variance	8.15	11.12	10.95	11.72	16.75

Factor loadings ≥0.5 are in bold face. Factor loadings <0.5 are in bold italics.

tions. Table 3 shows the five calculated factors and the associated factor loadings for the entire data set. The five factors account for 59% of the variance in the data set.

The five factors and the elements with high loadings that strongly influence them, in order of decreasing amount of variance that they explain, are as follows:

1. Factor 5 (Igneous Rock Factor): Al, K, Ga, Fe, Be, Sc, Co, Bi, Cu, Ni
2. Factor 4 (Black Shale Factor): Cd, Zn, Mo, V, Ag, Ni, U, Cu, Se
3. Factor 2 (Stibnite Factor): Cr, Sb
4. Factor 3 (Gold Factor): Hg, Tl, Au, As, Te, Sb
5. Factor 1 (Phosphate Factor): P, U, La

In addition, correspondence analysis was completed using DATAVIEW 07 (Carr, 2002). Correspondence analysis is a method used to graphically display unbiased relationships be-

tween variables. The axes of the graph are made perpendicular so that elemental relationships are not distorted. This is done via eigen decomposition which yields eigen vectors that define perpendicular axes. The principal components with the highest eigen values represent the most data and are referred to as factors 1 and 2. The graphs, which can be found in Patterson (2009), show a loose cluster of Au, Tl, As, Hg, and Te. Sb plotted away from all the other elements. The remaining elements formed a fairly tight cluster, with Ag, S, and W being closest to As, Hg, and Te, but still far from Au and Tl.

Effect of Supergene Oxidation

In order to test whether supergene oxidation had any effect on the statistical analysis of the dataset and the spatial distribution of the elements presented below, the multi-element dataset was combined with Yukon-Nevada Gold Corp.'s drill hole database, which has logging data on oxidation. Of the 6,416 samples in the Saval dataset, 4,832 samples do not have any logged supergene oxidation. Oxidation is mainly in the form of goethite and hematite along fracture surfaces. Figure 5 shows oxidized samples are present throughout the district but are more common in or very near the vertical projection of the open pit deposits, which is to be expected because mineralized decarbonatized, pyritic rocks are much more susceptible to supergene oxidation than weakly mineralized, carbonate-bearing rocks. Nevertheless, as Figure 5 shows, significant amounts of unoxidized samples occur in close proximity to oxidized samples within the vertical projection of the open pit deposits. In comparison, the Murray, SSX, and Smith underground deposits have fewer oxidized samples.

To further test whether or not elements were remobilized during supergene oxidation, the distributions of Au, Tl, Hg, As, Sb, Fe, Zn, and U concentrations for unoxidized and oxidized samples were compared by generating bar and whisker diagrams (Figure 6). Gold and Hg concentrations tend to be higher in unoxidized samples compared to oxidized samples, whereas Tl, As, and Sb concentrations tend to be higher in oxidized samples. Despite goethite and limonite occurring along fractures and appearing exotic rather than idigneous, there is no apparent difference in the distribution of Fe concentrations between unoxidized and oxidized samples, suggesting Fe has only moved short distances. Zinc, which is mobile, has slightly higher concentrations in oxidized samples, whereas U, which is highly immobile in a reducing environment, has higher concentrations in the unoxidized samples.

Though the bar and whisker diagrams between oxidized and unoxidized rocks show some potentially significant differences, it is difficult to determine whether those differences are truly due to supergene oxidation. Given 75% of the samples in the dataset are unoxidized and that unoxidized and oxidized samples are fairly well intermingled spatially, we concluded that supergene oxidation has had little to no effect on the statistical associations or the spatial distribution of the elements, and
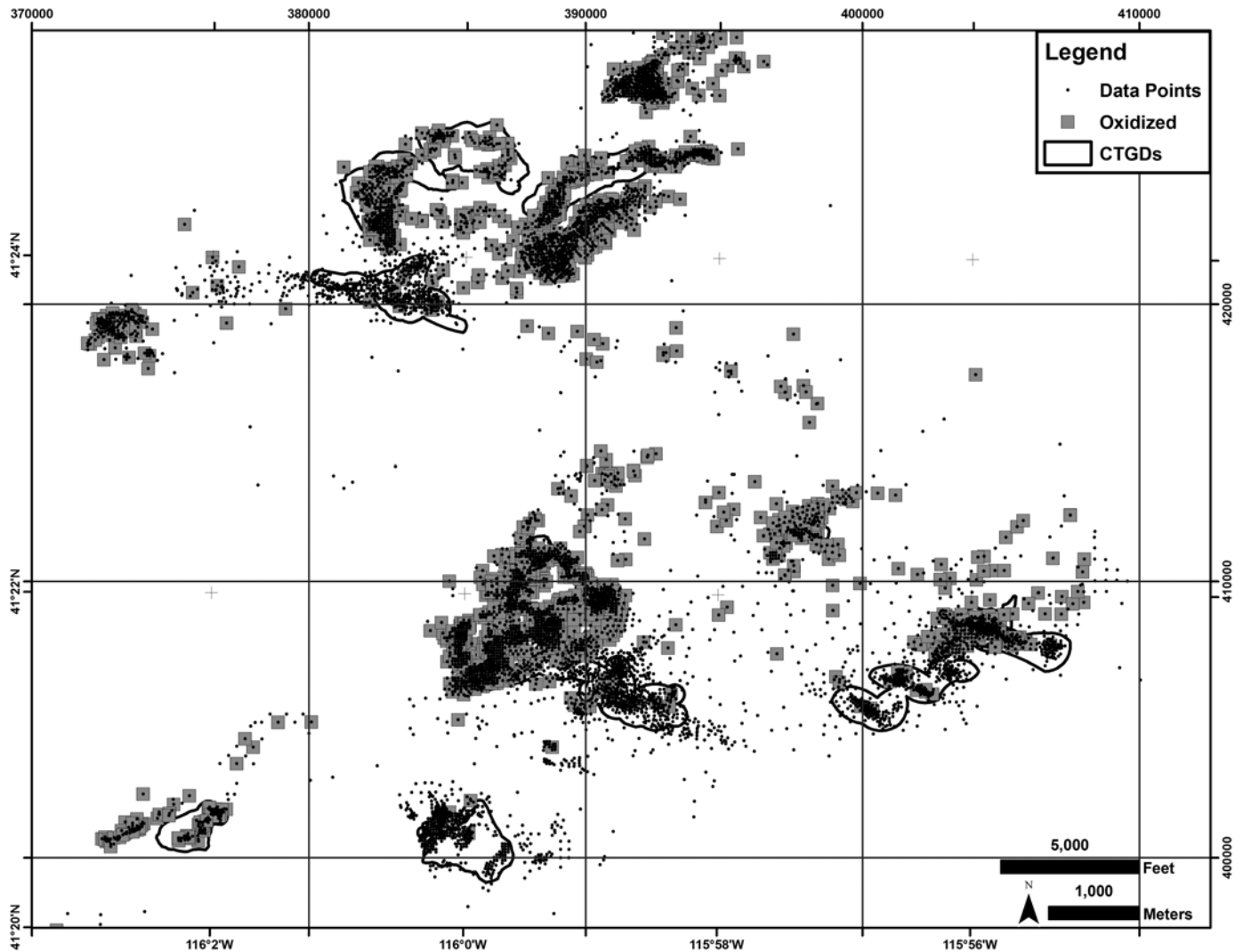
Figure 5. Map showing location of oxidized samples (gray squares) relative to the entire Saval data set (black dots) and CTGDs (black outlines). Coordinates are longitude-latitude (tics, degrees-minutes, WGS84) and local Jerritt Canyon mine grid (grid lines, feet, NAD27 Nevada West State Plane modified by a false northing of −2,000,000 ft).

that the observed patterns have not been significantly affected by weathering.

Summary of Elemental Associations

CTGD-related Elements

The statistical techniques applied to the Saval dataset identified a strong association between Au, Hg, Tl, and As, and, to a lesser degree, Te. Also, Sb and Ag show a weak association with these Au-related elements. The results are similar to other statistical studies of multi-element analyses from individual CTGDs at Jerritt Canyon. For example, Hofstra (1994) utilized factor analysis on samples taken from the North Generator deposit to identify a Au-As-Sb-Tl-Hg association that also included, to a lesser degree, Al, Be, Co, K and S. Dewitt (1999) utilized correlation coefficients to demonstrate a Au-Hg-As-Tl association at the SSX deposit, and like the

Saval data set, a much weaker correlation with Sb and Ag. Hofstra (1994) and Dewitt (1999) did not report Te analyses. Hutcherson (2002) collected and analyzed 85 samples from the Murray deposit and, using correlations coefficients, demonstrated a strong Au-Ag-Tl-Te-Hg-As-Sn association, but no association with Sb. These studies, unlike this study, did not restrict sampling to a single stratigraphic unit.

Carbonate-related Elements

Some of the strongest negative correlations in the Saval dataset occur with Ca, Mg, Sr, and to a lesser degree Mn. These elements occur in calcite and dolomite, which are important constituents in the DSrm. Importantly, these elements show negative correlation coefficients with CTGD-related elements, and, except for Mn, negative loadings in Factor 3 (the gold factor). The negative correlation directly reflects carbonate dissolution during formation of the CTGDs at Jerritt Canyon. Cal-

Lucia M. Patterson and John L. Muntean
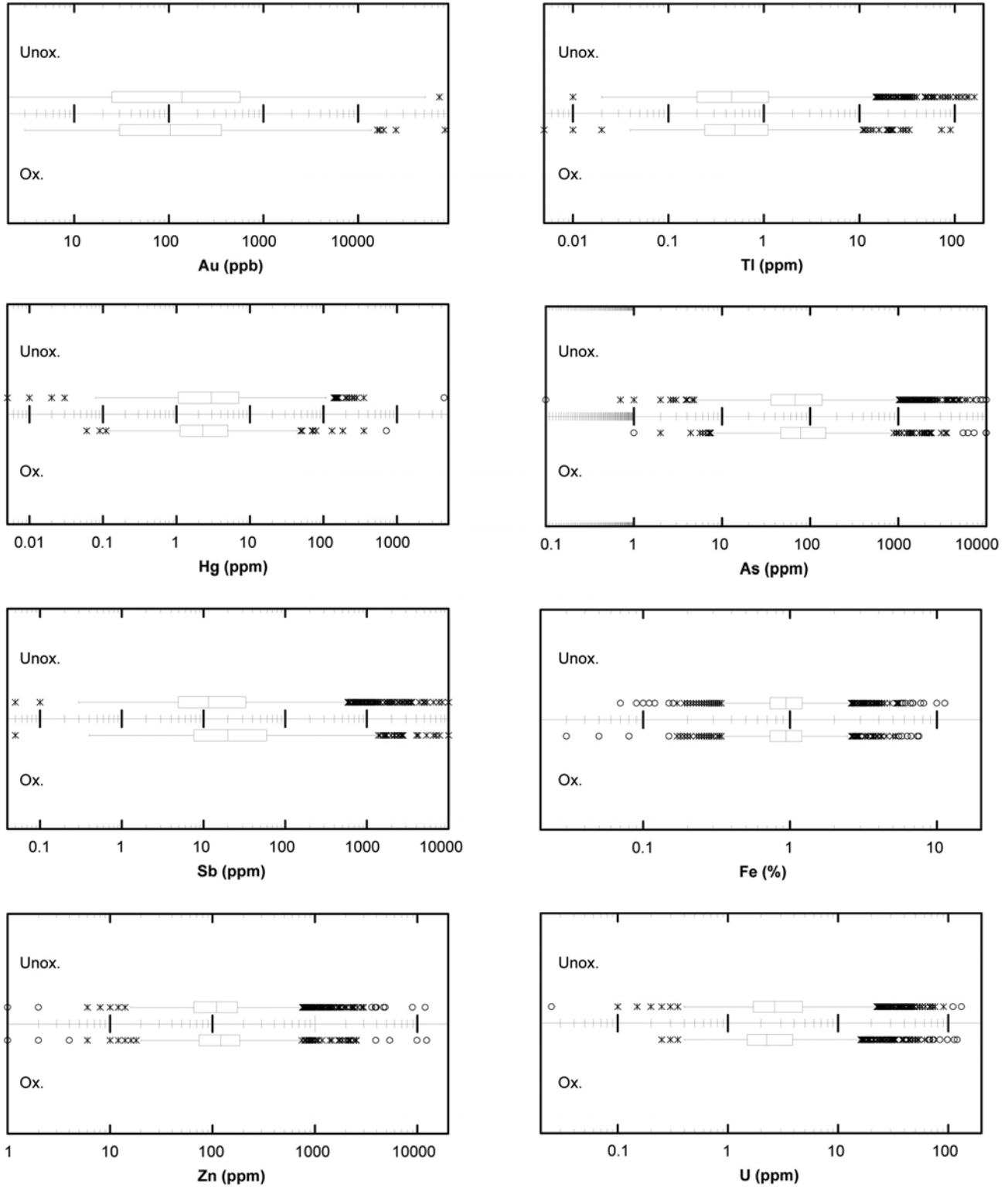
Figure 6. Bar and whisker diagrams for Au, Tl, Hg, As, Sb, Fe, Zn, and U. For each element, the upper bar and whisker diagram represents unoxidized samples (Unox.), and the lower diagram represents oxidized samples (Ox.). The center vertical line of the bar represents the median, and the length of each bar shows the range within which the central 50% of the values fall, with the ends of the bars at the first and third quartiles. The ends of the lines represent the lower and upper inner fence. The lower inner fence = the first quartilte – (1.5•(third quartile – first quartile) and the upper inner fence = the third quartile – (1.5•(third quartile – first quartile). The asterisks extend out to lower and upper outer fence. The lower outer fence = the first quartile – (3•(third quartile - first quartile) and the upper outer fence = the third quartile – (3•(third quartile – first quartile). Values beyond the outer fences are plotted as empty circles and are considered outliers. See text for interpretation.

cium also has negative correlation coefficients with Ag, Bi, Cu, Mo, Ni, P, U, and Zn, though not as strongly negative as with the CTGD-related elements (Figure 4).

Stibnite-related Elements

Although Sb weakly correlates with the CTGD-related elements, factor analysis (Factor 2) and correspondence analysis suggest Sb is isolated from the other elements. Stibnite is common in many of the CTGDs at Jerritt Canyon, but is not a reliable indicator of ore. It is a late-ore stage mineral that post-dates deposition of Au-bearing arsenian pyrite and marcasite. It commonly occurs in strongly silicified rock, where it fills fractures and vugs and cements breccias, commonly with drusy quartz, barite, and late calcite (Hofstra, 1994; Hutcherson, 2002). In the Saval data set, Sb shows no correlation with Ba, likely because barite is only partially dissolved in the nitric acid-aqua regia digestion. The association of stibnite with strong silicification is supported by the very strong negative loadings in Factor 2 for Ca, Mg, Sr, and Mn, indicating replacement of much of the calcite and dolomite by quartz (Table 3). In addition, Table 3 shows high loadings for Cr, and to a lesser extent W, which might be reflecting rock hardness and sample preparation by drilling and crushing with chromium steel and tungsten carbide tools.

Phosphate-related elements

A strong P-U-La association is indicated by their high loadings in Factor 1 (Table 3) and high correlation coefficients. As pointed out by Patterson (2009), phosphate lenses, consisting of apatite, are common in the bottom 10 feet of the DSrm. Uranium and La commonly occur as trace elements in apatite. However, Ca had a very low correlation coefficient with P. This is caused by Ca predominantly occurring in calcite and dolomite, which are far more abundant than apatite in the DSrm. Although not as strong, V and Ga also had high loadings for Factor 1 and correlation coefficients of ≥0.4 with P, U, and La. Uranium and La substitute for Ca in the apatite structure, while V readily substitutes for P.

Black shale-related elements

The statistical analyses identified a large group of mainly redox-sensitive elements that are commonly enriched in the organic component of many black shales worldwide. These "black shale-related elements" (BSEs) have high loadings for Factor 4 and include Cd, Zn, Mo, V, Ag, Ni, U, Se, and Cu (Table 3). These elements are mostly transported as chloride, oxide, anionic and hydroxide complexes in oxidized aqueous fluids (Rose, 1980).

Igneous rock-related elements

Factor 5 in Table 3 indicates an association between Al, K, Ga, Fe, Be, Sc, Co, Bi, Cu, Ni, and to a lesser extent, V and Zn. These elements are commonly associated with mafic igneous rocks. Patterson (2009) noted that some of the analyzed 5 foot intervals in the Saval dataset contained narrow dikes of late Mississippian basalt/andesite. Berillium and Bi, however, suggest the presence of felsic rocks, though none were observed.

SPATIAL PATTERNS

Point maps of the elements were produced first in order to look for patterns in elemental distribution in and around areas of known mineralization. Each element was displayed in ESRI's GIS software package, ArcMap, as point maps, color-coded by concentration. Concentration ranges for each color were determined from breaks in slope or inflection points in logarithmic cumulative distribution curves for each individual element. Figure 7 shows the point map for Au. Note the significant amount of variation in the gold assays among closely spaced points. Though point maps are critical in assessing specific localities, the vast amount of data and high local variance made it difficult to distinguish elemental patterns at the district-scale.

Gridded maps of the data better reveal the spatial patterns in the elements. The gridded maps were made in ArcMap using Target software, an add-on to ArcMap developed by Geosoft. The grids were created by kriging using a spherical variogram model and a cell size of 150 feet and search radius of 1,500 feet. Once grids were made, they were displayed in ArcMap as classified images with discrete changes in the colors representing breaks in the population of a given element, which were determined from the histogram of each grid. We caution that model diagnostics for the gridding were not run; therefore, some patterns may be misleading, especially in areas of low data density along the margins of the grids.

Gold

Figure 8 shows the distribution of Au. Two types of patterns relative to the known deposits are apparent based on values ≥50 ppb Au: 1) narrow, commonly linear, patterns with sharp gradients in the Murray/Winters Creek area, and 2) broad diffuse patterns in the SSX/Smith area. The narrow linear type of pattern is best exemplified by the Murray deposit. Au values ≥50 ppb exhibit a west-northwest linear trend through the Murray deposit, which extends westward into the northern portion of the Wright Window area. This trend is 14,000 feet long and about 800 feet wide and follows the New Deep Fault (Figures 3 and 8). Another example is at the West Generator deposit, where a zone of ≥50 ppb Au is 4,000 feet long and 900 feet wide. The Marlboro Canyon deposit exhibits a northeast trend of ≥50 ppb Au that is roughly 5,000 feet long and 1,700 feet wide. Similarly, the Winters Creek deposit occurs in a parallel, northeast-trending zone of discontinuous ≥50 ppb Au zones that is 9,000 feet long and 1,000 feet wide; however much of the vertical projection of Winters Creek occurs in a zone that has <50 ppb Au. In contrast, a large, broad area of ≥50 ppb Au, which is about 2,000 feet wide, extends 25,000 feet west-northwest from the Dash and Smith deposits to the Steer and Saval deposits. The few holes in the Cow Canyon area in the hanging wall of the Mill Creek fault
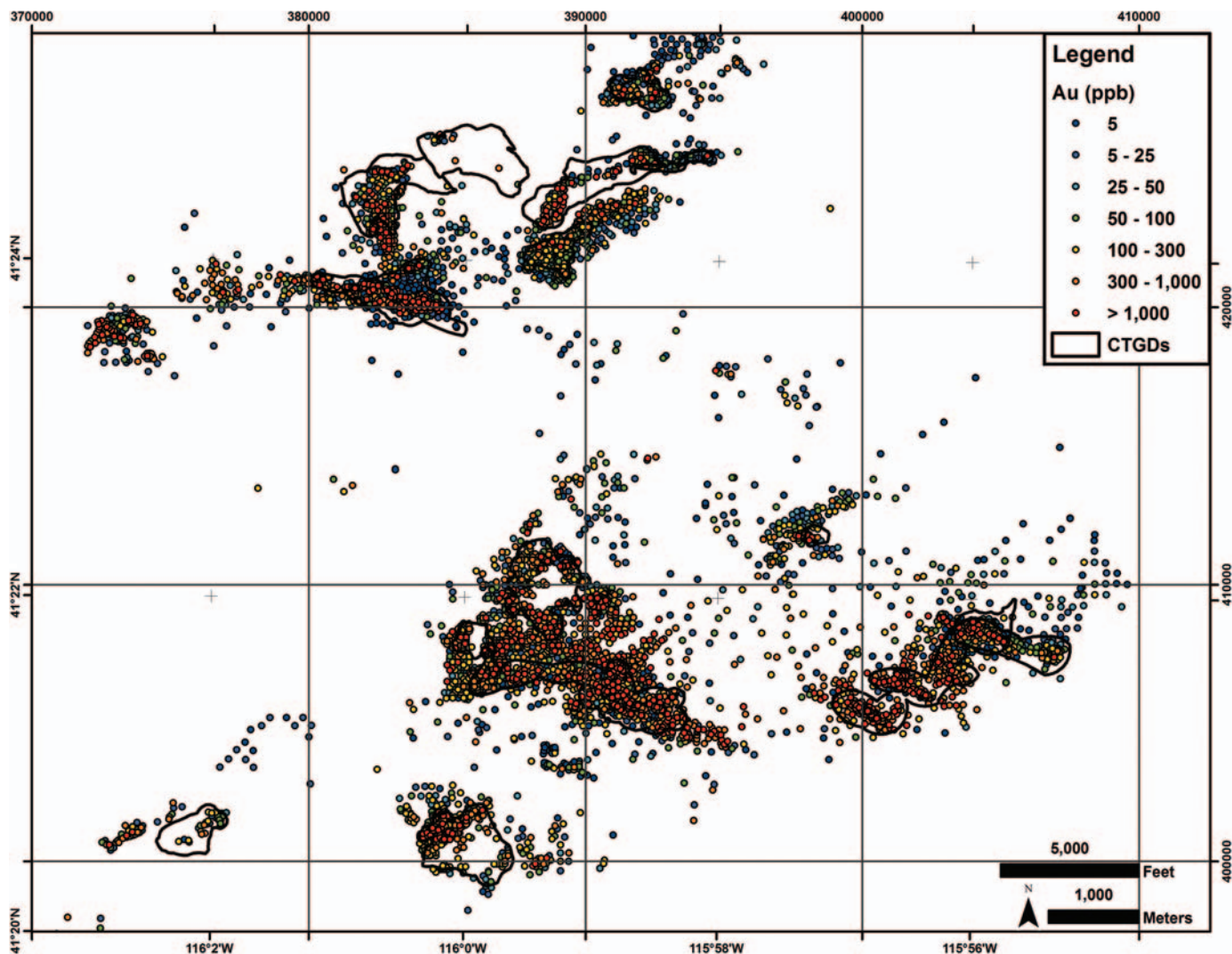
Figure 7. Point map for Au. Also shown are outlines of the CTGDs (faint gray lines). Coordinates are longitude-latitude (tics, degrees-minutes, WGS84) and local Jerritt Canyon mine grid (grid lines, feet, NAD27 Nevada West State Plane modified by a false northing of -2,000,000 ft).

suggest the trend may continue another 20,000 feet to Wright Window (Figures 3 and 8). Gold values are clearly much more extensive and continuous in the SSX/Smith area than in the Murray/Winters Creek area. Within the large, diffuse zone of the SSX/Smith area, there are a few distinct northeast-trending zones, including along the Mill Creek Fault. Note the sharp truncation of Au values by the South Boundary Fault (Figures 3 and 8). South of the South Boundary Fault, is another, much narrower, west-northwest zone of ≥50 ppb Au associated with the Burns Basin deposit, which is localized at the intersection of a west-northwest basalt/andesite dike swarm and the northeast trending Sb/Purple fault zone (Figures 3 and 8).

Similarly, higher gold grades are more restricted in the Murray/Winters Creek area compared to the SSX/Smith area. The area of ≥100 ppb Au in the SSX/Smith area is almost as large as large as the zone of ≥50 ppb Au. However, higher grades do not form continuous halos to the deposits. For example,

zones of ≥300 ppb Au form discontinuous pods up to a few thousand feet outboard of deposits in the SSX/Smith area, but occur mainly within the vertical projection of the deposits in the Murray/Winters Creek area. An exception is a continuous northeast-trending zone on east side of SSX.

CTGD-related Elements

As demonstrated above, Hg, Tl, As, Te, and Sb are the elements most closely associated with Au. Figure 9 shows the grids for these elements. The 50 ppb and 300 ppb Au contours are shown for comparison.

Tl

Of the CTGD-related elements, Tl forms a pattern most similar to Au (Figure 9A). Thallium values of ≥0.3 ppm in the Murray/Winters Creek lie almost entirely within the 50 ppb Au

contour and are mostly restricted to the vertical projection of the deposits. On the other hand, the 0.3 ppm Tl contours cover a large, pervasive area in the SSX/Smith area that is larger than the 50 ppb Au contour. With regard to higher Tl values, the largest, most continuous zone of ≥1 ppm Tl is not spatially associated with the known deposits, but rather occurs along a northwest trend extending from the Smith deposit to the Marlboro Canyon deposit. The zone is about 20,000 feet long and 3,000 feet wide, and in detail, is comprised of smaller northeast- and west-north-west-trending zones. Thallium values ≥2 ppm are strictly confined to areas of ≥300 ppb Au. Like Au, Tl values are truncated by the South Boundary Fault.

Hg

Gridded values of ≥1 ppm Hg occur throughout much of the Murray/Winters Creek area and most of SSX/Smith area (Figure 9B). Values of ≥1 ppm Hg are approximately coincident with the 50 ppb Au contour in the Murray/Winters Creek area; however, almost the entire SSX/Smith area is covered by ≥1 ppm Hg, and, like the 1 ppm Tl contour, extends from the Smith deposit to the Marlboro Canyon deposit. Unlike the other CTGD-related elements, the ≥1 ppm Hg zone extends 2,000 feet southward beyond the South Boundary Fault. In the vicinity of the Steer, Saval, SSX, Smith, and Dash deposits, zones of ≥3 ppm Hg extend up to 2,000 feet beyond the 50 ppb Au contour.

As

Gridded values of ≥10 ppm As occur throughout the entire Murray/Winters Creek and SSX/Smith areas (Figure 9C). In the Murray/Winters Creeks area, zones of ≥50 ppm As locally ex-
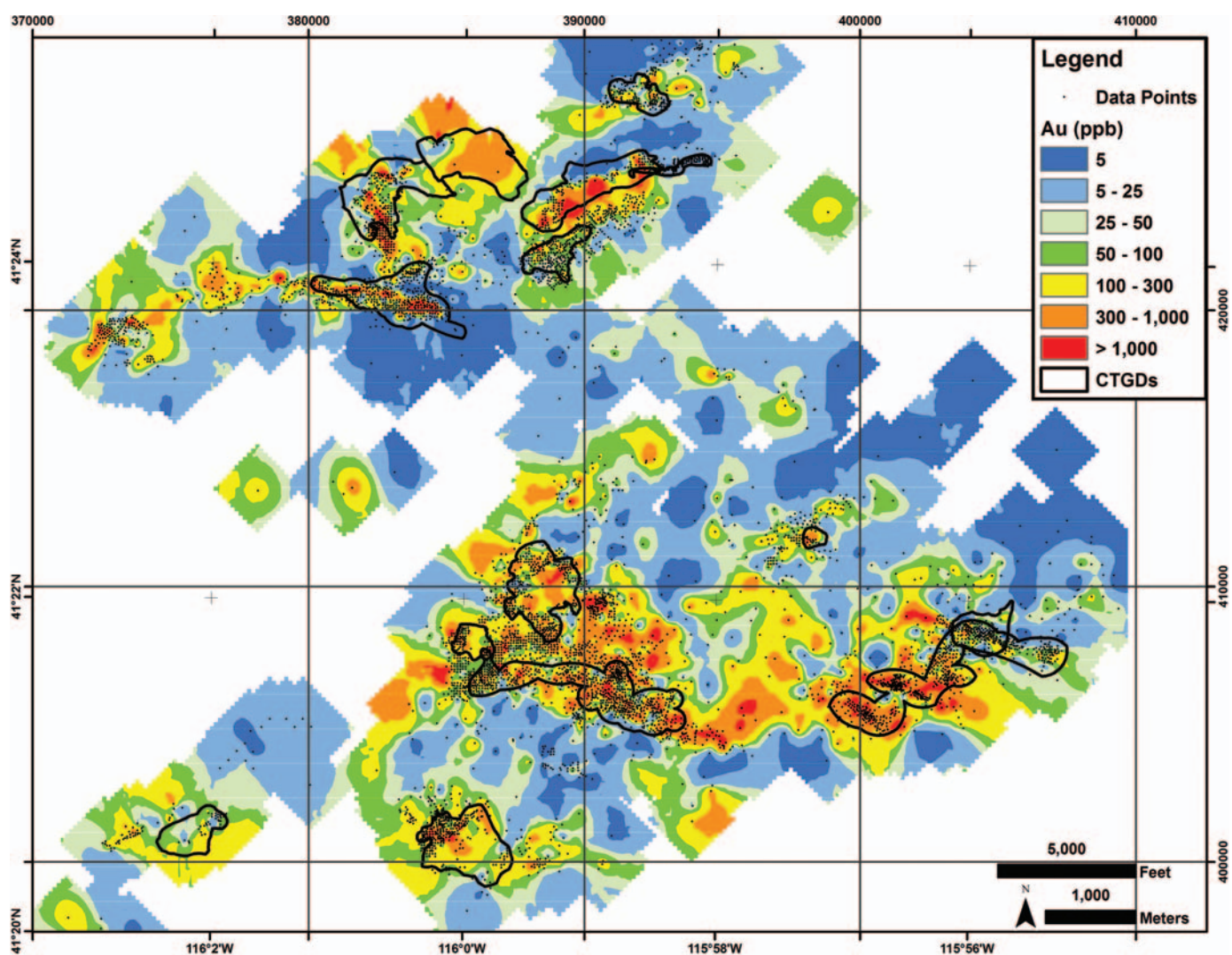
Figure 8. Map of gridded Au values. Also shows location of the 300 ppb Au contours (thick black lines), the 50 ppb Au contours (thin back lines), outlines of the CTGDs (white lines) and the surface projection of the Saval data points (black dots). The legend is for the gridded values, not the actual values. Coordinates are longitude-latitude (tics, degrees-minutes, WGS84) and local Jerritt Canyon mine grid (grid lines, feet, NAD27 Nevada West State Plane modified by a false northing of -2,000,000 ft).
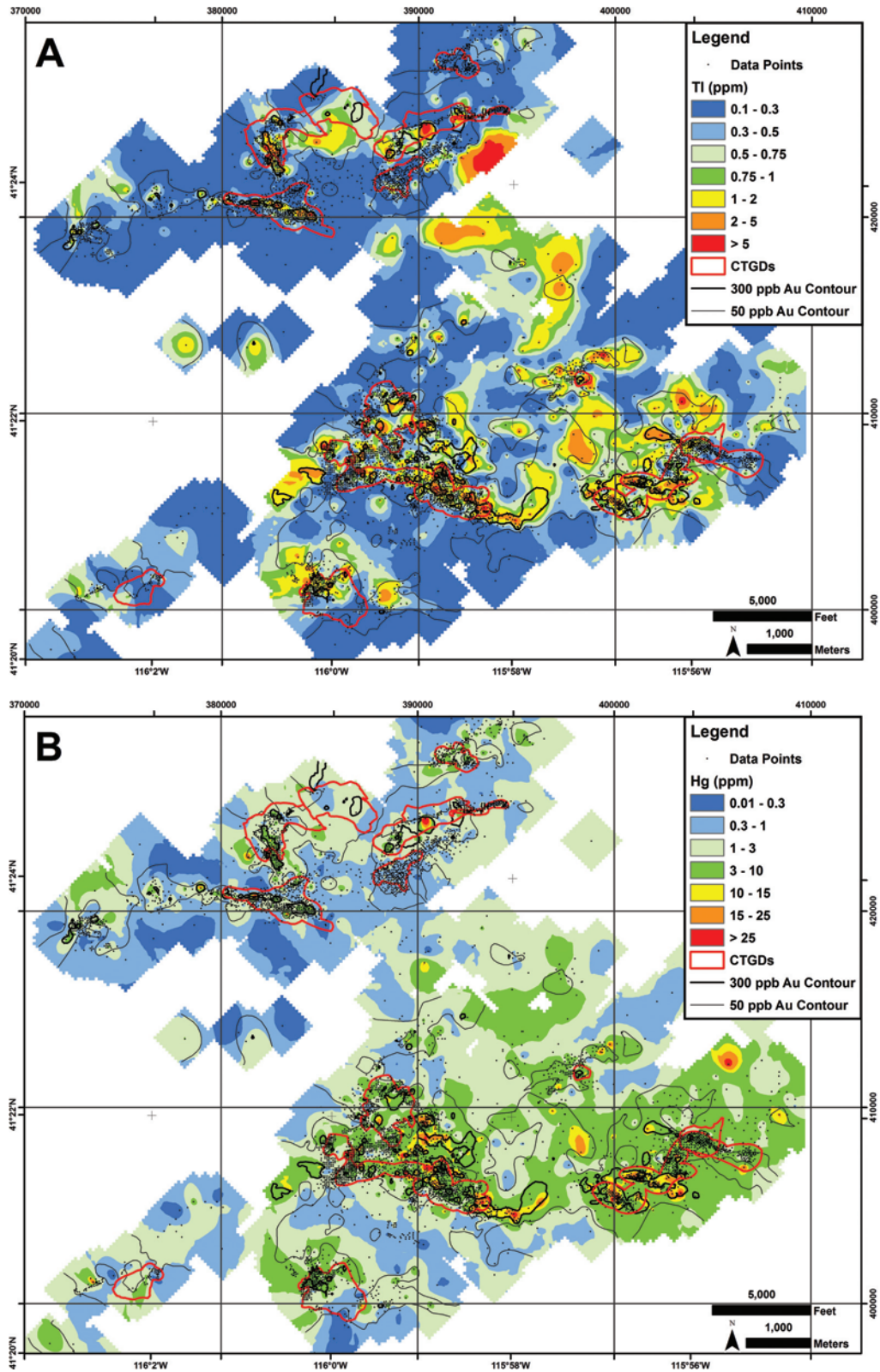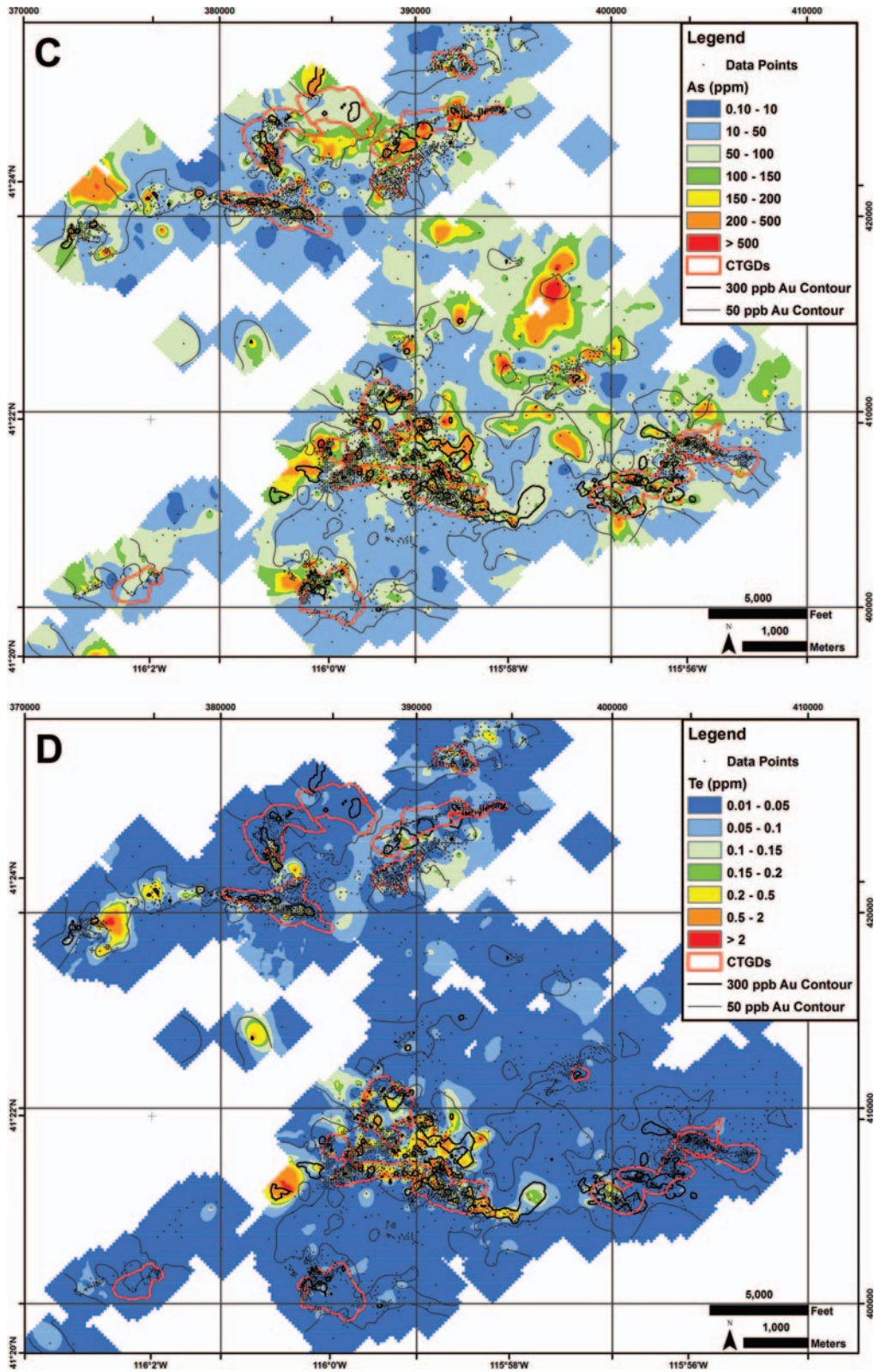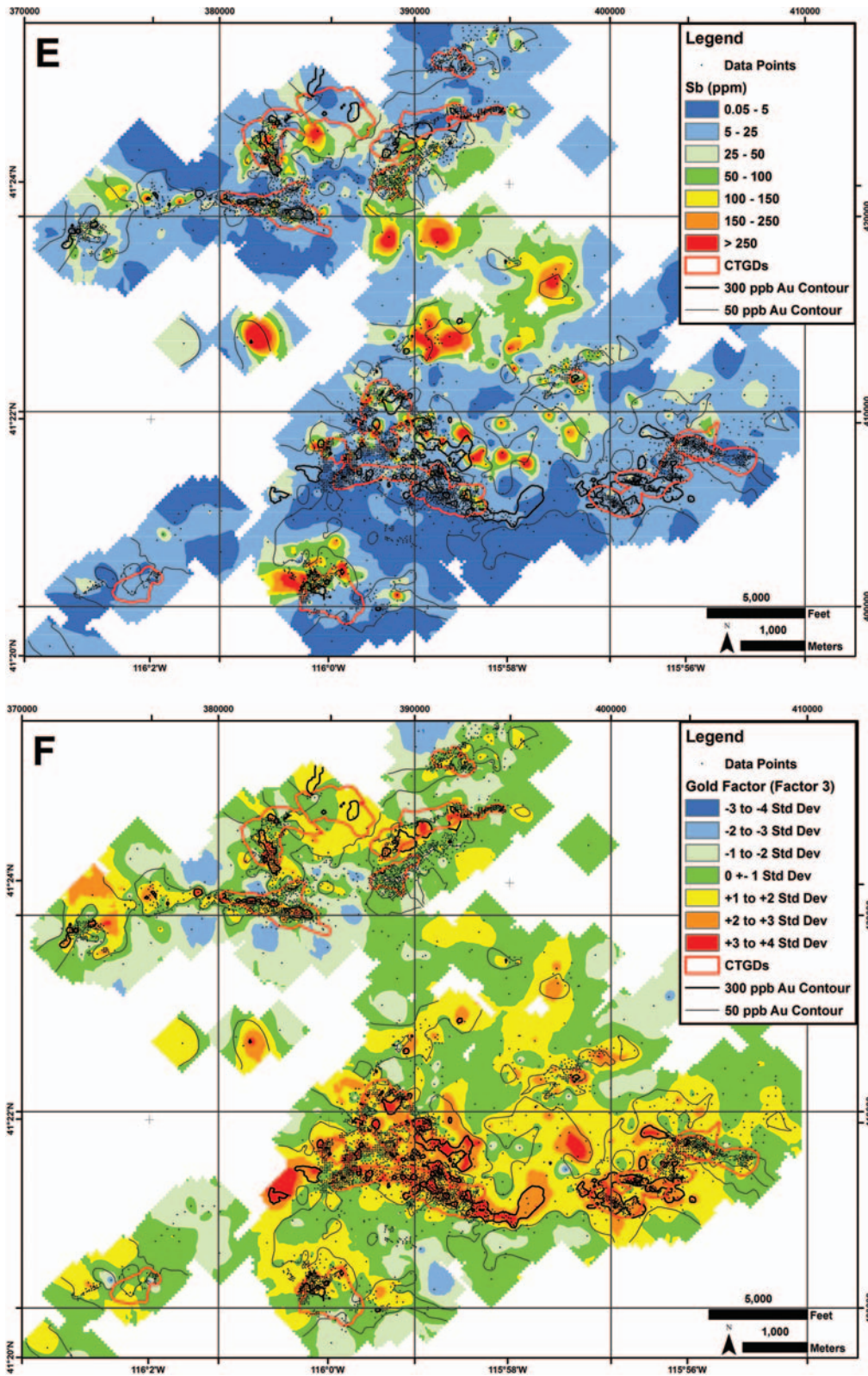
Figure 9. Maps of gridded values of CTGD-related trace elements and factor scores. A. Tl, B. Hg, C. As, D. Te, E. Sb, and F. Au Factor scores (classified as standard deviations above and below the mean), as described in the text. Also shows locations of the 300 ppb Au contours (thick black lines), the 50 ppb Au contours (thin back lines), outlines of the CTGDs (red lines) and the surface projection of the Saval data points (black dots). The legends are for the gridded values, not the actual values. Coordinates are longitude-latitude (tics, degrees-minutes, WGS84) and local Jerritt Canyon mine grid (grid lines, feet, NAD27 Nevada West State Plane modified by a false northing of -2,000,000 ft).

Figure 9 (continued). Maps of gridded values of CTGD-related trace elements and factor scores. A. Tl, B. Hg, C. As, D. Te, E. Sb, and F. Au Factor scores (classified as standard deviations above and below the mean), as described in the text. Also shows locations of the 300 ppb Au contours (thick black lines), the 50 ppb Au contours (thin back lines), outlines of the CTGDs (red lines) and the surface projection of the Saval data points (black dots). The legends are for the gridded values, not the actual values. Coordinates are longitude-latitude (tics, degrees-minutes, WGS84) and local Jerritt Canyon mine grid (grid lines, feet, NAD27 Nevada West State Plane modified by a false northing of -2,000,000 ft).

Figure 9 (continued). Maps of gridded values of CTGD-related trace elements and factor scores. A. Tl, B. Hg, C. As, D. Te, E. Sb, and F. Au Factor scores (classified as standard deviations above and below the mean), as described in the text. Also shows locations of the 300 ppb Au contours (thick black lines), the 50 ppb Au contours (thin back lines), outlines of the CTGDs (red lines) and the surface projection of the Saval data points (black dots). The legends are for the gridded values, not the actual values. Coordinates are longitude-latitude (tics, degrees-minutes, WGS84) and local Jerritt Canyon mine grid (grid lines, feet, NAD27 Nevada West State Plane modified by a false northing of -2,000,000 ft).

tend beyond, but mostly occur within the 50 ppb Au contour. Zones of ≥50 ppm As are fairly coincident with the 50 ppb Au contour in the area around the Steer, Saval, and SSX deposits; however, like Tl and Hg, zones of ≥50 ppm As extend for several thousand feet beyond the 50 ppb Au contour in the northwest zone that extends from the Smith deposit to the Marlboro Canyon deposit. Locally, gridded As values are 500 ppm in that zone, well beyond the 50 ppb Au contour. Like Au and Tl, As values are truncated by the South Boundary Fault.

Te

Of all the CTGD-related elements, Te values are the least elevated (lower values than Au) and most restricted (Figure 9D). The largest zone of elevated Te occurs in the area around the Steer, Saval, and SSX deposits, where the 0.05 ppm Te contour is fairly coincident with the 50 ppb Au contour. Elevated Te values ≥0.2 ppm locally occur in the Cow Canyon and Wright Window areas, suggesting, as did Au, that a west-northwest zone of elevated CTGD-related elements extends 20,000 feet from the Steer deposit to Wright Window. Tellurium values are also truncated by the South Boundary Fault. The highest Te values in the Murray/Winters Creek area form a discontinuous linear trend along the New Deep Fault that is 5,000 feet long and 600 feet wide, extending through the Murray deposit. Tellurium values ≥0.05 ppm are present in and around the Marlboro Canyon and Winters Creek deposits in broad east-northeast trends.

Sb

As indicated above, Sb exhibits a weaker statistical association with Au than the other CTGD-related elements and occurs as stibnite, which is a late ore-stage mineral. Therefore, it is not surprising the spatial pattern of Sb is very different from Au, Tl, Hg, As and Te (Figure 9E). Antimony values of ≥5 ppm are present throughout much of the Murray/Winters Creek and SSX/Smith areas. However, most zones of ≥50 ppm Sb occur outside zones of ≥300 ppb Au, with some of the more persistently high values occurring in the zone of high Tl, Hg, and As between the California Mountain and Marlboro Canyon deposits.

Ratios

Ratios between the CTGD-related elements were also calculated and gridded to see if patterns existed proximal to the known deposits, especially donut-like patterns surrounding the deposits. Such patterns in ratios might exist if there were differing budgets of CTGD-related elements in the fluid or differing controls on the solubility of the CTGD-related elements in the fluid. For example, if a greater amount of As was in the fluid than Au, or if As was more soluble in the fluid than Au for a given set of P-T-X conditions, much of it might remain in the fluid for a greater distance than Au before precipitating, thus producing a donut of high As/Au ratios surrounding the deposit. Such zoning of metals is common in porphyry copper systems. Unfortunately, maps of the gridded ratios showed no distinct,

consistent patterns. Examples of the gridded ratio maps can be found in Patterson (2009).

Gold Factor Scores

Figure 9F is an image of the gridded values of the factor scores for Factor 3—the Gold Factor discussed above (Table 3). Factor scores were calculated for each sample of the Saval dataset by summing the products of the concentration and Factor 3 loading for each element. Plotting gold factor scores on cross-sections or on maps enables one to seek out zones of high statistical association between Au-related trace elements, even in the absence of high Au values. For example, if Tl, Hg, As, Te, and Sb values are high in a given area where Au values are low, high Gold Factor scores may still be present. Like the gridded images for the individual gold-related elements, high Factor 3 scores are more spatially restricted in the Murray/Winters Creek area and show the same narrow, west-northwest trend through the Murray mine which tails off to Wright Window along the New Deep Fault. The SSX-Smith area shows a much more extensive, continuous zone of high Factor 3 scores, and, also shows a prominent northeast-trend of high scores located northwest of the California Mountain deposit. That trend appears to be the northeastern extension of the Purple Fault zone in the SSX mine. The northeast trend extends to the eastern extension of the New Deep Fault (Figures 3 and 9F).

Elements related to CTGD Alteration

As pointed out above, decarbonatization and silicification are the main alteration types associated with the CTGDs at Jerritt Canyon. Therefore, areas of depleted Ca, Mg, and Sr are good proxies for identifying localities where decarbonatization has taken place, especially if comparing analyses of a single lithology as in the Saval dataset. Figure 10A clearly shows Ca is depleted around the deposits. Magnesium and Sr are also depleted, as shown by Patterson (2009). With the exception of the Winters Creek deposit, Ca is mostly <8 wt%, Mg is mostly <3.5 wt%, and Sr is mostly <80 ppm where Au values are ≥50 ppb in the Murray/Winters Creek area. In the SSX/Smith area, Ca is mostly <11%, Mg is mostly <5 wt%, and Sr is mostly <80 ppm, where Au values are ≥50 ppb. The patterns are accentuated when ratios are applied. Zones with Ca/Au ratios of <4,000 are coincident with to slightly larger than the 50 ppb Au contour (Figure 10B). However, the patterns of Ca and Ca/Au do not show consistent gradients towards the vertical projections of the deposit, and their patterns, in detail, are quite complicated.

Other Elements

Consistent with the conclusions drawn from the statistical analyses, the spatial patterns of the others elements are much different than those of gold and the other CTGD-related elements. Patterns for P, U, V, Zn, Mo, Ni, Bi, Se, Cu, and Ag are
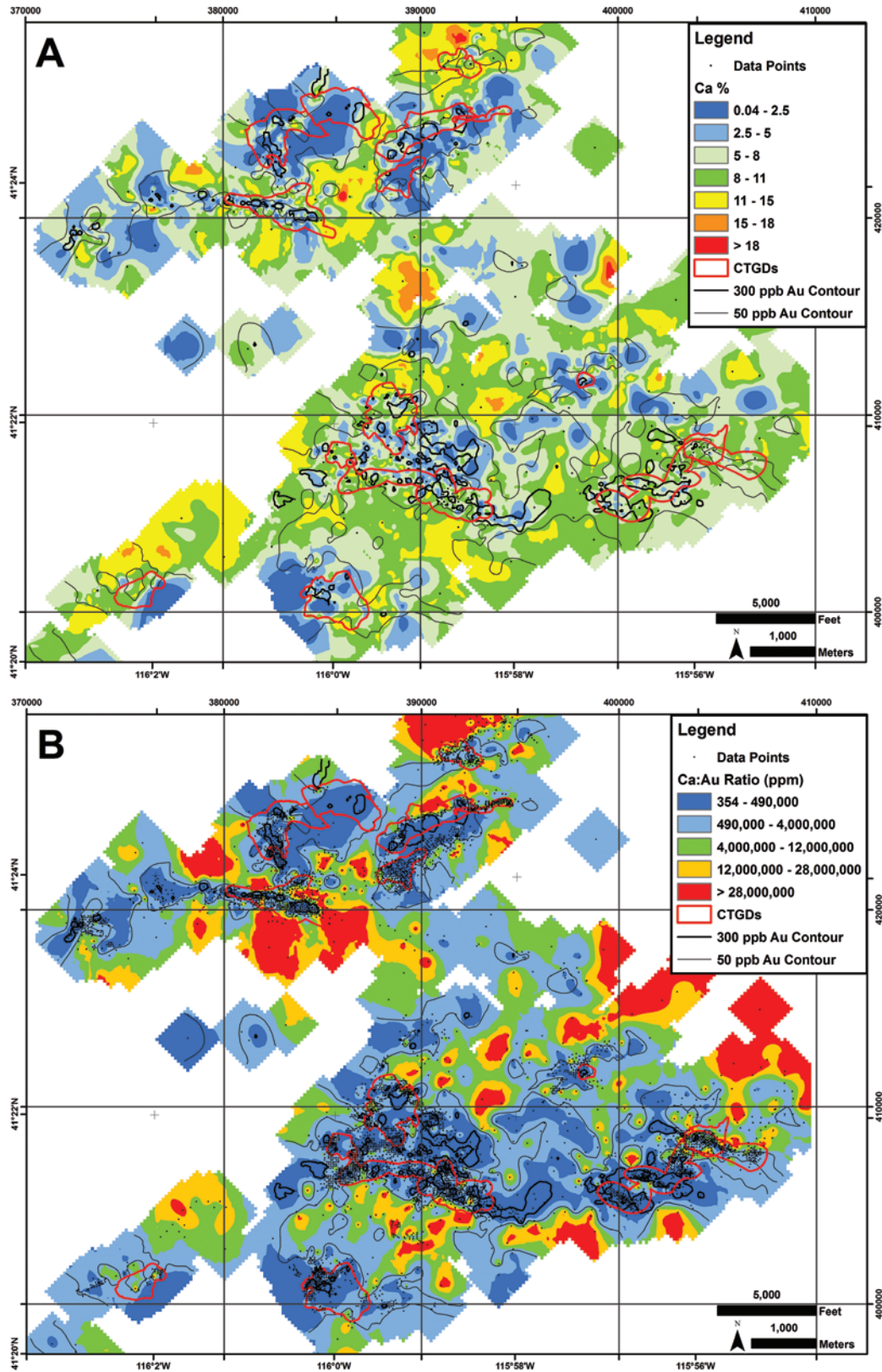
Figure 10. Maps of gridded values of A. Ca, and B. Ca/Au. Also shows locations of the 300 ppb Au contours (thick black lines), the 50 ppb Au contours (thin back lines), outlines of the CTGDs (red lines) and the surface projection of the Saval data points (black dots). The legends are for the gridded values, not the actual values. Coordinates are longitude-latitude (tics, degrees-minutes, WGS84) and local Jerritt Canyon mine grid (grid lines, feet, NAD27 Nevada West State Plane modified by a false northing of -2,000,000 ft).

shown in Figure 11. Cadmium is not shown but shows very similar patterns to Zn (Patterson, 2009), consistent with its strong statistical correlation with Zn. Cadmium commonly substitutes for Zn in sphalerite. Patterns for other elements not shown in Figure 11 are in Patterson (2009). A common theme observed is that almost all the elements, other than the CTGD-related elements, are elevated around the Winters Creek deposit.

Phosphate Elements

Figure 11A clearly shows the Murray/Winters Creek area is characterized by a northeast zone of elevated P, which is commonly ≥2000 ppm. The SSX/Smith area, on the other hand, is mostly <2000 ppm P and shows no distinct patterns. Lanthanum (Patterson, 2009) and U (Figure 11B) show similar patterns in the Murray/Winters Creek area, as does the factor scores for Factor 1—the Phosphate Factor (Figure 12A). As pointed out above, the base of the DSrm commonly has phosphate lenses, whose formation Patterson (2009) attributed to upwelling cold waters during rapid transgression following the subaerial exposure and karsting of the SOhc that the marks Saval unconformity. The reason for elevated phosphate in the Murray/Winters Creek area, relative to the SSX/Smith area is unclear. Patterson (2009) logged a subset of the Saval dataset, and found that the 34 holes that had phosphate lenses out of the 247 holes that were logged did not preferentially occur in the Murray/Winters Creek area.

Black Shale Elements

The gridded images for some of the "black shale elements", including U, V, Zn, Mo, Ni, Bi, Se, Cu, and Ag are shown in Figures 11B-J. These elements commonly exhibit high concentrations in the vicinity of the Burns Basin and especially at the Winters Creek deposit. High Ni, Bi, Cu and Pb also occur across a large area north of the California Mountain deposit near the eastern extension of the New Deep Fault. As pointed out above, this area is also high in CTGD-related elements and appears to be the northeastern extension of the Purple Fault zone. Murray is the only deposit where "black shale elements" share a similar spatial pattern to the CTGD-related elements. The "black shale elements" are all locally elevated in the vicinity of the SSX and Smith deposits, but do not exhibit any coherent pattern. This is the case for most of the areas outside Winters Creek and Burns Basin. This is clearly shown in the gridded image of factor scores for Factor 4—the Black Shale Factor, which shows distinct highs centered on the Winters Creek and the Burns Basin deposits (Figure 12B). The apparent northeastern extension of high scores from Burns Basin appears to be related to edge effects during gridding. Patterson (2009) attributed the "black shale element" anomalies to migration of an oxidized basinal brine that was associated with hydrocarbon migration in the Jerritt Canyon district in the late Paleozoic or early Mesozoic.

As pointed out above, Ag has a weak statistical association with Au and the other CTGD-related elements, but shows a much stronger association with the "black shale elements". Sil-ver does exhibit a spatial distribution similar to Au in the SSX/Smith areas; however, unlike Au, Tl and As, it is not truncated by the South Boundary Fault (Figure 10J). The Ag:Au ratio of ore at Jerritt Canyon is <1, and Ag has not been detected in Au-bearing pyrite using laser ablation ICP analyses (A. Hofstra, unpublished data reported in appendix of Cline *et al.*, 2005). However, Hutcherson (2002) demonstrated Ag correlated with Au in limited sample transects across ore zones in the Murray deposit. We conclude that minor Ag was likely associated with Au mineralization, but that most of the Ag is pre-ore.

DISCUSSION

Extent of Hydrothermal System associated with CTGDs at Jerritt Canyon

Statistical analysis and gridded maps of individual elements from the Saval dataset indicate a Au-Tl-Hg-As-Te signature was associated with formation of CTGDs at Jerritt Canyon. Antimony is associated with the CTGDs in the form of late-stage stibnite, but has a much weaker statistical association and does not share the same spatial patterns observed in the other CTGD-related elements. Published elemental signatures of CTGDs from other districts include:

1. Deep Star (Heitt et al, 2003): Au, As, Hg, Sb, Tl, W, ±Ag, Zn
2. Turquoise Ridge (Cassinerio and Muntean, 2010): Au, Hg, As, W, S, Tl, Sb, Te
3. Goldstrike (Bettles, 2002): Au, As, Hg, Sb, Tl, S, ±Ag, Te

It is important to note that the statistical analyses and spatial patterns presented in this paper only take space, and not time, into account. Elements may be spatially related, but may not have been deposited at the same time from the same hydrothermal system. However, the very similar spatial patterns shared between Au, Tl, Hg, and As at Jerritt Canyon are compelling evidence that these metals were deposited at the same time from the same hydrothermal system. Contemporaneous deposition of these metals is supported by laser ablation ICP analyses of ore-stage pyrites from Jerritt Canyon that show a Au-Tl-Hg-As-Pb-Cu-Sb association (A. Hofstra, unpublished data reported in appendix of Cline *et al.*, 2005). At Turquoise Ridge electron microprobe analyses of ore-stage pyrite show a Au-As-Tl-Hg-Cu-Te-Sb signature (Longo et al, 2009), which begs the question why Cu is not statistically or spatially related to gold at Jerritt Canyon. The reason is that Cu concentrations in the pyrite are about the same as the concentration of Au in the pyrite. The estimated background Cu and Au values in the Saval dataset are 14 ppm and 2.5 ppb, respectively (Table 2). Thus, formation of ore-stage pyrite containing similar concentrations of Cu and Au will not have much of an effect on the pre-ore Cu content of the rock; therefore, one should not expect a statistical association in the Saval dataset. Apparent associations between Au and other metals, such as Cu, Pb, Zn, Bi, and Mo, in other
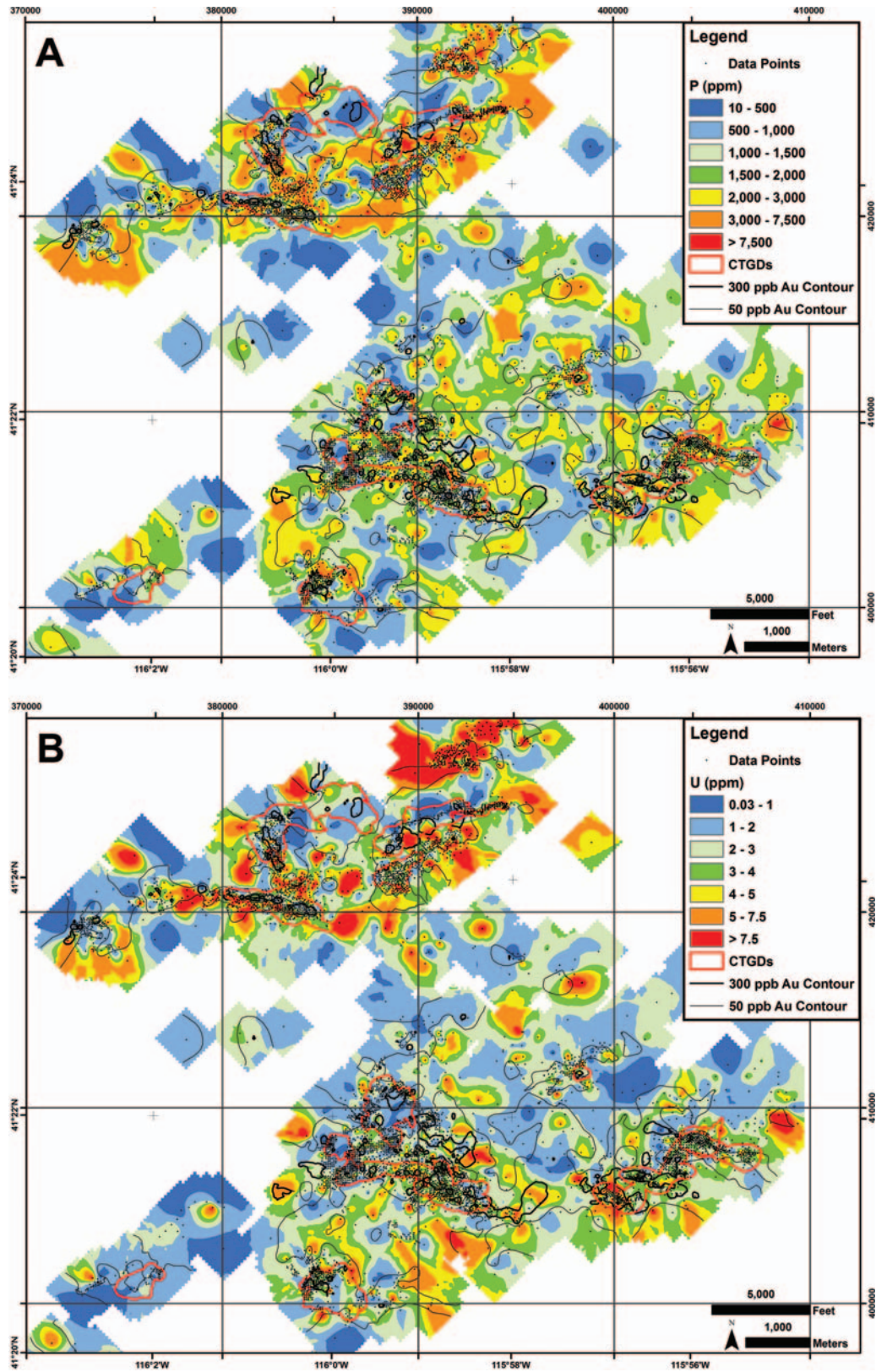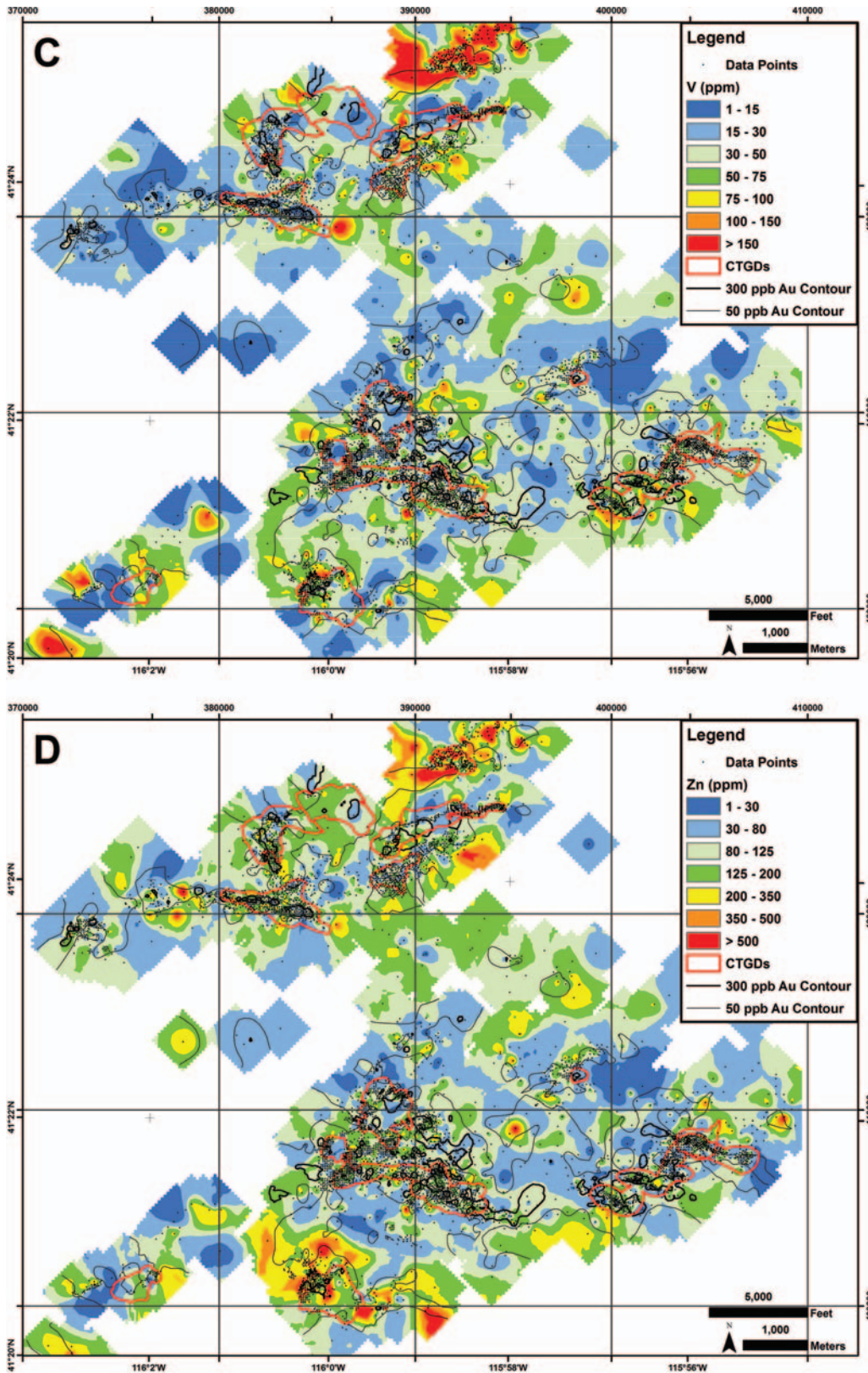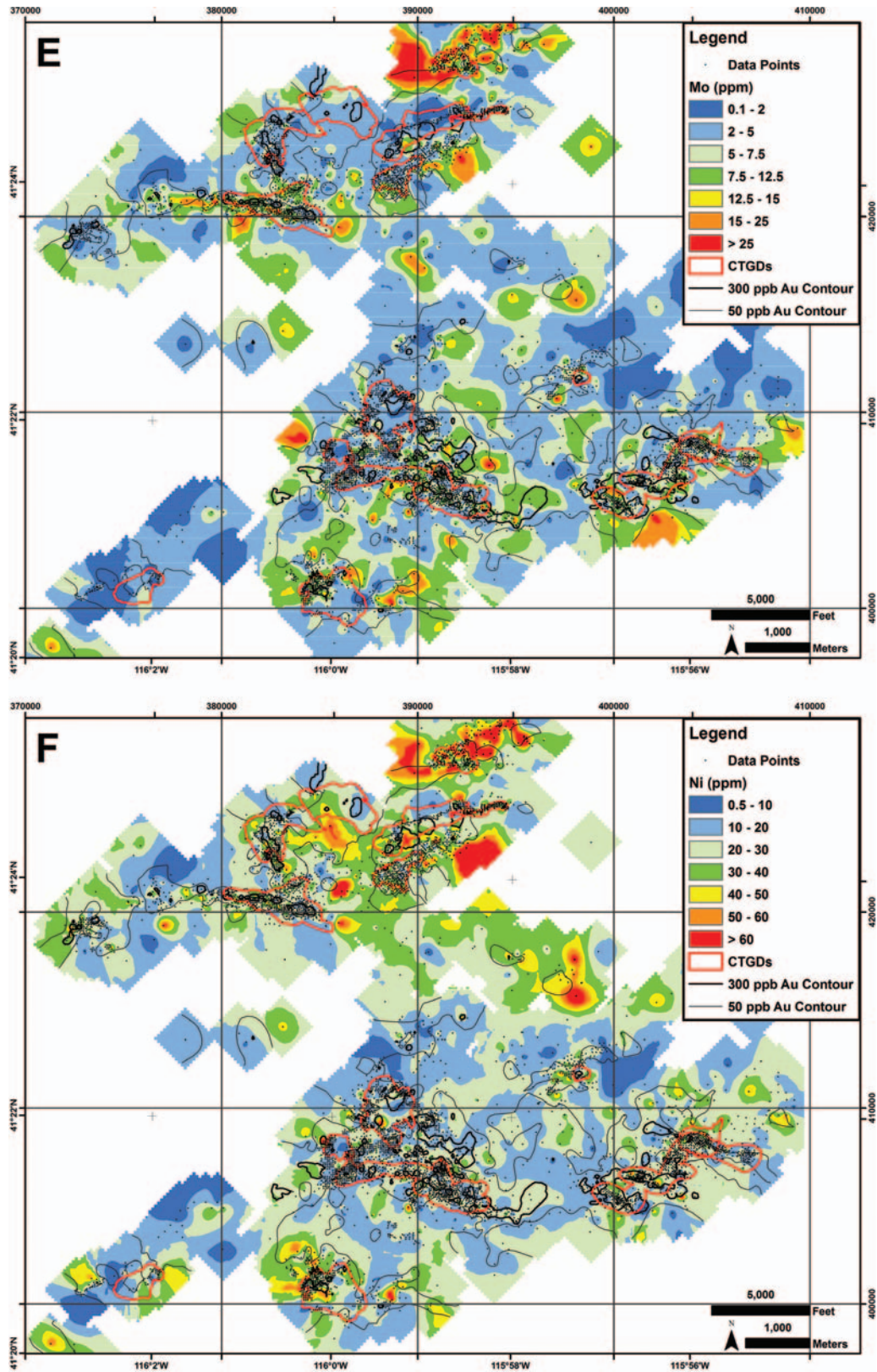
Figure 11. Maps of gridded values of "Phosphate" and "Black Shale" elements as discussed in the text. A. P, B. U, C. V, D. Zn, E. Mo, F. Ni, G. Bi, H. Se, I. Cu, and J. Ag. Also shows locations of the 300 ppb Au contours (thick black lines), the 50 ppb Au contours (thin back lines), outlines of the CTGDs (red lines) and the surface projection of the Saval data points (black dots). The legends are for the gridded values, not the actual values. Coordinates are longitude-latitude (tics, degrees-minutes, WGS84) and local Jerritt Canyon mine grid (grid lines, feet, NAD27 Nevada West State Plane modified by a false northing of -2,000,000 ft).
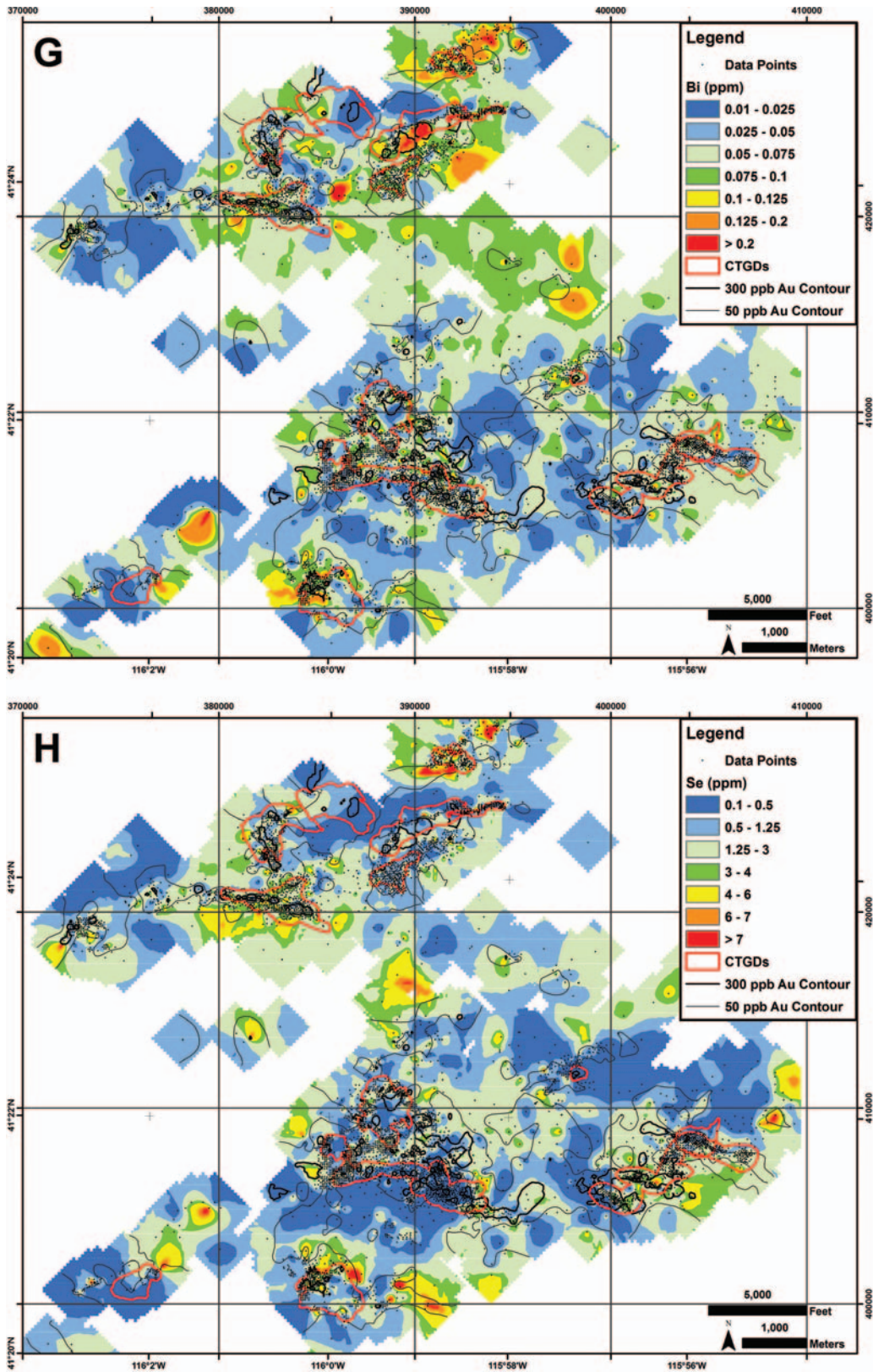
Figure 11 (continued). Maps of gridded values of "Phosphate" and "Black Shale" elements as discussed in the text. A. P, B. U, C. V, D. Zn, E. Mo, F. Ni, G. Bi, H. Se, I. Cu, and J. Ag. Also shows locations of the 300 ppb Au contours (thick black lines), the 50 ppb Au contours (thin back lines), outlines of the CTGDs (red lines) and the surface projection of the Saval data points (black dots). The legends are for the gridded values, not the actual values. Coordinates are longitude-latitude (tics, degrees-minutes, WGS84) and local Jerritt Canyon mine grid (grid lines, feet, NAD27 Nevada West State Plane modified by a false northing of -2,000,000 ft).
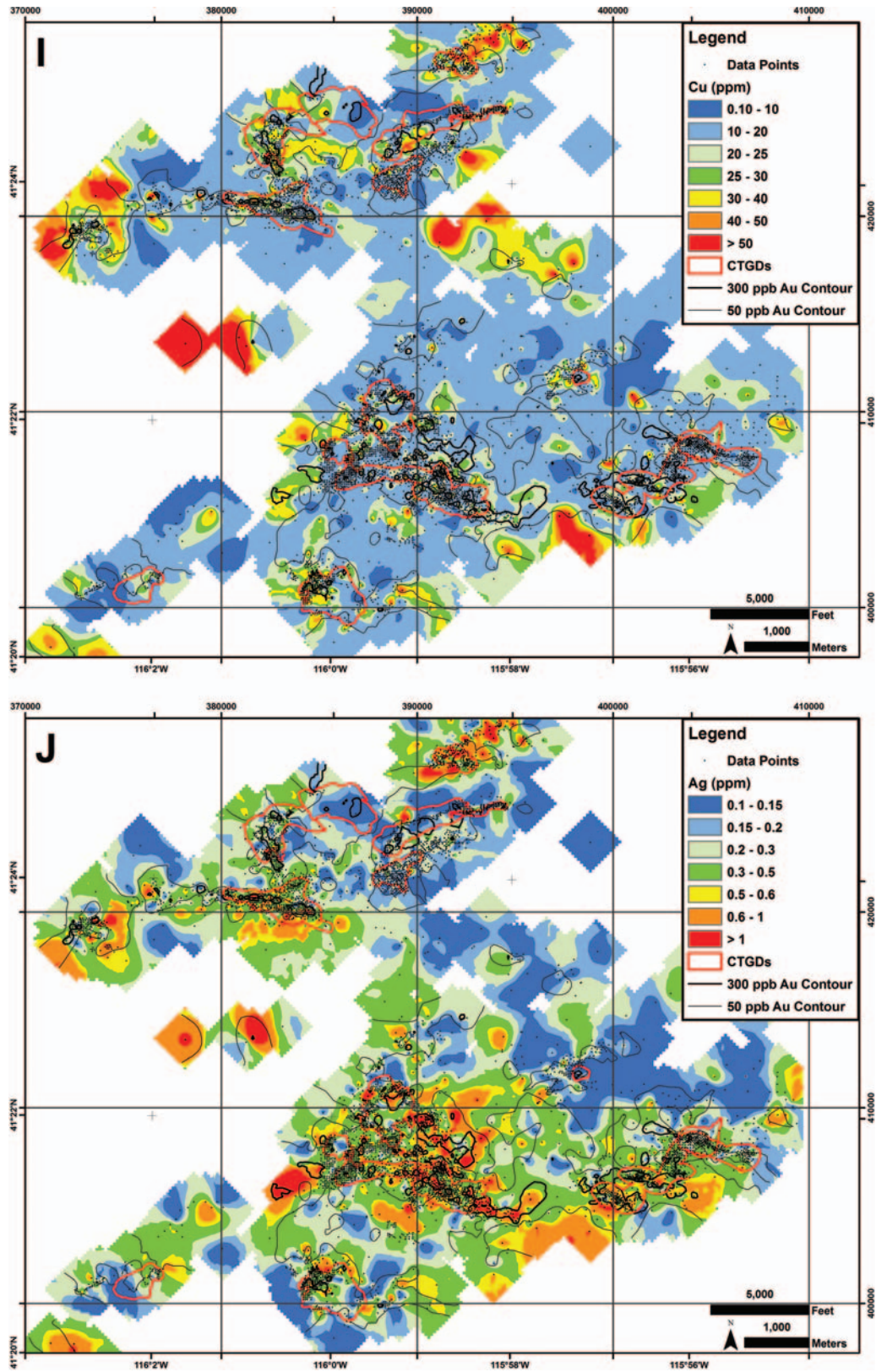
Figure 11 (continued). Maps of gridded values of "Phosphate" and "Black Shale" elements as discussed in the text. A. P, B. U, C. V, D. Zn, E. Mo, F. Ni, G. Bi, H. Se, I. Cu, and J. Ag. Also shows locations of the 300 ppb Au contours (thick black lines), the 50 ppb Au contours (thin back lines), outlines of the CTGDs (red lines) and the surface projection of the Saval data points (black dots). The legends are for the gridded values, not the actual values. Coordinates are longitude-latitude (tics, degrees-minutes, WGS84) and local Jerritt Canyon mine grid (grid lines, feet, NAD27 Nevada West State Plane modified by a false northing of -2,000,000 ft).
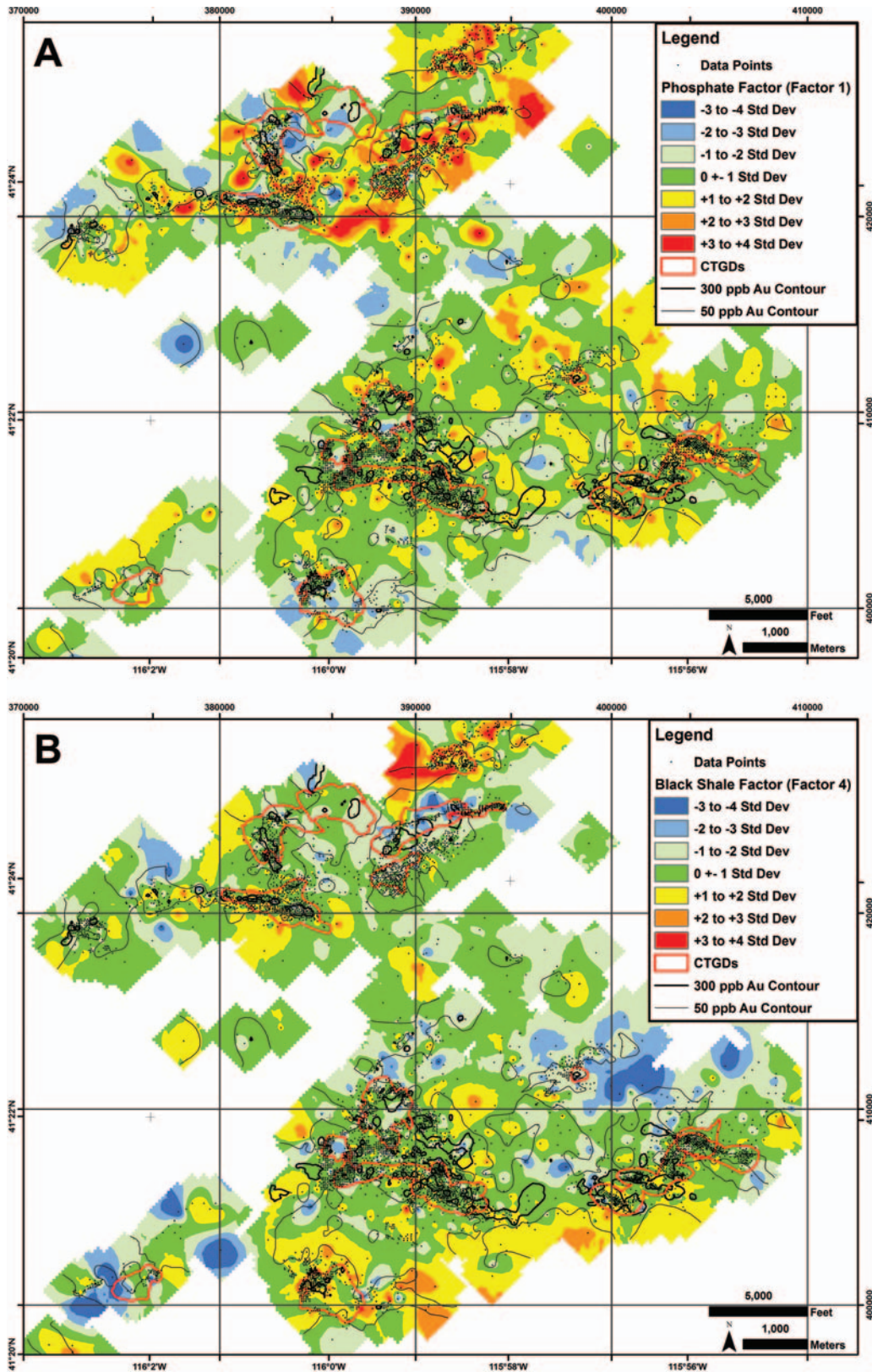
Figure 11 (continued). Maps of gridded values of "Phosphate" and "Black Shale" elements as discussed in the text. A. P, B. U, C. V, D. Zn, E. Mo, F. Ni, G. Bi, H. Se, I. Cu, and J. Ag. Also shows locations of the 300 ppb Au contours (thick black lines), the 50 ppb Au contours (thin back lines), outlines of the CTGDs (red lines) and the surface projection of the Saval data points (black dots). The legends are for the gridded values, not the actual values. Coordinates are longitude-latitude (tics, degrees-minutes, WGS84) and local Jerritt Canyon mine grid (grid lines, feet, NAD27 Nevada West State Plane modified by a false northing of -2,000,000 ft).

Figure 11 (continued). Maps of gridded values of "Phosphate" and "Black Shale" elements as discussed in the text. A. P, B. U, C. V, D. Zn, E. Mo, F. Ni, G. Bi, H. Se, I. Cu, and J. Ag. Also shows locations of the 300 ppb Au contours (thick black lines), the 50 ppb Au contours (thin back lines), outlines of the CTGDs (red lines) and the surface projection of the Saval data points (black dots). The legends are for the gridded values, not the actual values. Coordinates are longitude-latitude (tics, degrees-minutes, WGS84) and local Jerritt Canyon mine grid (grid lines, feet, NAD27 Nevada West State Plane modified by a false northing of -2,000,000 ft).

Figure 12. Maps of gridded factor scores for A. "Phosphate Factor", and B. "Black Shale Factor", classified as standard deviations above and below the mean. Also shows locations of the 300 ppb Au contours (thick black lines), the 50 ppb Au contours (thin back lines), outlines of the CTGDs (red lines) and the surface projection of the Saval data points (black dots). The legends are for the gridded values, not the actual values. Coordinates are longitude-latitude (tics, degrees-minutes, WGS84) and local Jerritt Canyon mine grid (grid lines, feet, NAD27 Nevada West State Plane modified by a false northing of -2,000,000 ft).

CTGDs have to be evaluated with caution because many CTGDs, such as those in the northern Carlin trend, Cortez, and Getchell, are spatially associated with Mesozoic granitic intrusions. As pointed out above, no evidence exists for pre-Eocene felsic magmatism prior to formation of the CTGDs at Jerritt Canyon; thus simplifying interpretation of the Saval dataset.

Halos of CTGD-related elements are summarized in Table 4. Anomalous Au (≥50 ppb), Tl (≥0.5 ppm), Hg (≥1 ppm), As (≥50 ppm), and Factor 3 (Gold Factor) scores extend up to several thousand feet along the Saval discontinuity, laterally from the vertical projection of CTGDs at Jerritt Canyon. It should be noted that the halos in Table 4 are likely maxima; some of the halos to known deposits might be actually be more proximal to undiscovered deposits. Also, it should be stressed that these halos are based on gridded data. Point maps for Au (Figure 6) and other elements commonly show high values intermingled with low values. Gridding the data smooths out the variability, but the gridded images presented in this paper are still quite complex. No simple bull's eye-type patterns were found. The elements showed no distinct zoning patterns, as one might see in epithermal or porphyry systems. For example, the Eocene-age Bingham Canyon porphyry system in Utah zones outward from a Mo-rich core, to Cu-Au to Pb-Zn to Au-As in a distance ranging from 13,000 to 30,000 feet (Babcock *et al.*, 1995). In contrast, at Jerritt Canyon, the geochemical signature related to Eocene gold mineralization does not change over a minimum distance of 40,000 feet. Au, Tl, Hg, and As attenuate irregularly from individual CTGDs at about the same rate, suggesting the elements had similar depositional mechanisms that resulted from a shared fluid pathway in pressure-temperature-composition space. An exception is Sb, whose distribution relative to the CTGDs is not consistent and is controlled by the deposition of late-stage stibnite, driven by rapid cooling during collapse of the hydrothermal system at Jerritt Canyon (Hofstra *et al.*, 1991).

The variability in the CTGD-related elements in and around the deposits at Jerritt Canyon suggests complicated, fracture controlled fluid flow along the Saval discontinuity. Rather than fluid upwelling along a few major faults and moving thousands of feet laterally along favorable stratigraphy or low-angle structural zones like the Saval, we envision multiple zones of passive upwelling fluids that rose along major-high-angle faults, such as the west-northwest faults that are occupied by late Mississippian dikes. The fluids were then distributed into complex arrays of secondary fracture systems and locally bled out hundreds of feet laterally into favorable lithologies or low-angle structures. This is best illustrated in the Murray/Winters Creek area, where mineralization is relatively restricted. For example, mineralization along the New Deep Fault at the Murray deposit extends out to the north end of Wright Window, forming a zone of anomalous CTGD-related elements that is 14,000 feet long, but only 800 feet wide. In contrast, the data suggest that the SSX/Smith area represents a large zone of upwelling hydrothermal fluids as defined by a relatively coherent 50 ppb Au contour that is about 25,000 feet long and 2,000 feet wide. In addition, the South Boundary Fault in the SSX/Smith area seems to have acted as a barrier to hydrothermal fluid flow. With the exception of Hg, all of the other CTGD-related elements are truncated against the fault, and there is little evidence for significant post-ore movement on the fault.

Within the large zone at SSX/Smith, the highest, most extensive Te values are centered on the SSX, Steer, and Saval deposits. Tellurium is commonly associated with epithermal deposits related to alkalic magmatism (cf. Jensen and Barton, 2000), as well as high-sulfidation epithermal deposits and CTGDs (cf. Kesler et al., 2003). Tellurium is a volatile element in basaltic melts (MacKenzie and Canil, 2008), and has been detected, along with Tl, in sublimates precipitated near active fumarole vents (Fulignati and Sbrana, 1998) and in sulfides in fresh pumice from Quaternary volcanoes (Larocque et al., 2008). Furthermore, vapor transport of Au, Cu, As and Sb are supported by analyses of coexisting hypersaline brine and va-

Table 4. SUMMARY OF HALOS.

Element	Relative to Vertical Projection of Deposit	Relative to 50 ppb Au contour
Au (50 ppb)	SSX/Smith: ≤2,400 feet (≤3,800 ft along strike)	na
	Murray/Winters Creek: ≤1,000 ft (≤4,000 ft along strike)	
Tl (0.5 ppm)	SSX/Smith: ≤6,000 ft	SSX/Smith: no halo
	Murray/Winters Creek: no halo	Murray/Winters Creek: no halo
Hg (1 ppm)	SSX/Smith: ≤6,000 ft	SSX/Smith: ≤2,500 ft
	Murray/Winters Creek: ≤2,000 ft	Murray/Winters Creek: ≤1,300 ft
As (50 ppm)	SSX/Smith: ≤6,000 ft	SSX/Smith: ≤1,600 ft
	Murray/Winters Creek: ≤1,400 ft (≤1,900 ft along strike)	Murray/Winters Creek: ≤1,200 ft
Te (0.05 ppm)	SSX/Smith: ≤2,400 ft (only in SSX area)	SSX/Smith: no halo
	Murray/Winters Creek: no halo	Murray/Winters Creek: no halo
Factor 3 Scores (Gold Factor) (≥1 Std Dev)	SSX/Smith: ≤6,800 ft	SSX/Smith: ≤1,700 ft
	Murray/Winters Creek: ≤600 ft (≤4,000 ft along strike)	Murray/Winters Creek: no halo
Ca (<8 wt%)	SSX/Smith: ≤2,400 ft (only in SSX area)	SSX/Smith: no halo
	Murray/Winters Creek: ≤1,400 ft (≤4,400 ft along strike)	Murray/Winters Creek: no halo

por-rich fluid inclusions, which represent immiscible magmatic-hydrothermal aqueous fluids trapped above 450°C and 300 bars, from porphyry copper and tin deposits. Some vapor-rich inclusions have high Au, Cu, As and Sb concentrations, locally higher than those in the brine (Heinrich et al., 1999). Heinrich (2005) proposed that vapor transport of Au and associated trace elements from a deep magmatic source (deeper than porphyry copper systems) could be a viable model for the formation of CTGDs. If magmatic vapor from an underlying source is responsible for mineralization at Jerritt Canyon, the main intrusion is likely beneath the SSX, Steer, and Saval deposits.

Applications to Exploration

The patterns in the Saval dataset presented in this paper should have applications in the exploration for CTGDs at Jerritt Canyon and in other districts. The 50 ppb Au contour appears to form the most coherent halo to the known CTGDs at Jerritt Canyon. Though Au continues to be the best vectoring tool to find Au, other CTGD-related elements form significant halos to the deposits, some of which form larger, more coherent halos than the 50 ppb Au contour, such as Hg and As (Table 4). Furthermore, if multiple types of hydrothermal systems of different ages and elemental signatures are present, multi-element analyses can be critical in distinguishing targeted Carlin-type mineralization from other types of Au mineralization that might contain elevated Ag and base metals. For example, Homestake Mining Company's discovery of the West Archimedes CTGD in the Eureka district was based on drilling beneath a prospect pit that yielded samples with anomalous Au, As, and Hg, but with low Ag and base metals, which are abundant in many of the mineralized occurrences in the district (Dilles *et al.*, 1996). In addition, Te might serve as important indicator of magmatic upwelling zones as discussed above.

If multi-element data is collected, factor analysis and calculation and plotting of factor scores should be routinely carried out. Factor analysis is a viable tool because high factor scores for a CTGD Factor (Factor 3 in Table 3) outline areas of potential where Au values might be low. For example, if individual Au values are low in a given area, but Hg, Tl, As, and Te values are high, the resultant factor scores will also be high, offering the possibility that higher gold values are present nearby. High factor scores that take into account all of the CTGD-related elements should be more robust than high values of individual elements. In districts with more than one hydrothermal elemental signature, such as juxtaposed Eocene CTGDs and Mesozoic intrusion-related signatures, factor analysis could generate separate factors that could be used to discriminate between the two hydrothermal systems.

Thousands of samples are not required to see the patterns displayed in Figures 8–12. To demonstrate this, we gridded the elemental values for CTGD-related elements using only 247 samples, which were from holes that were re-logged as de-

scribed by Patterson (2009). Figure 13 shows the gridded images for Au and As. Note their similarity to the maps in Figures 8 and 9C, respectively. The maps for Hg, Tl, and Te are similar as well, as shown by Patterson (2009). The results suggest hundreds of holes can show similar patterns as thousand of holes. The cost for combined Au assay and multi-element analyses is around $25/sample. Using the 247 samples to generate a geochemical grid similar to the maps shown in Figure 13 would cost $6,175. Several districts in Nevada have hundreds of exploration holes. However, one can legitimately argue that not all districts have a stratigraphic horizon analogous to the Saval, and thus thousands of analyses from the entire lengths of drill holes would likely be required. However, some stratigraphic horizons are known to have widespread anomalous trace elements in some districts. Examples include the contact between the Hamburg Dolomite and the Dunderberg Shale in the Eureka district, and the contact between the Devonian Devils Gate Limestone (or Guilmette Limestone) and Devonian/Mississippian siliciclastic units such as the Pilot Shale, Webb Formation or Woodruff Formation in several districts.

Finally we outline potential targets at Jerritt Canyon based soley on the Saval dataset and the compiled geology map of Muntean and Henry (2007) (Figure 14). The targets are summarized as follows:

1. *Mahala:* Located between the Smith and SSX deposits within the large west-northwest-trending zone of ≥50 ppb Au and strongly anomalous CTGD-related elements. The area contains numerous west-northwest-trending late Mississippian dikes. Drilling is relatively wide-spaced. Yukon-Nevada Gold Corp. had already been focusing their exploration effort in this area in recent years (Yukon-Nevada Gold Corp. press releases, 2007–2008).

2. *California Mountain:* Large northeast-trending area of strongly anomalous CTGD-related elements, but relatively low gold. It is located northwest of the California Mountain open pit in an area of sparsely drilled lower plate rocks.
    The area contains several potential intersections zones between the northeast projection of the Purple fault, an important ore-controlling structure in SSX deposit, and west-northwest faults, including the eastern extension of the New Deep fault zone.

3. *Murray NW Extension:* This target is the northwest extension of New Deep fault zone, which is the main ore control in the underground Murray deposit. It has similar concentrations of Au and CTGD-related elements as at Murray. Drilling is fairly wide-spaced for a likely narrow target, like the Murray deposit.

4. *New Deep East Extension:* This is the sparsely drilled east extension of the New Deep fault zone, just north of the Bidart anticline.

5. *Cow Canyon:* This area is the northwest projection of the large west-northwest-trending zone of ≥50 ppb Au and strongly anomalous concentrations of CTGD-related ele-
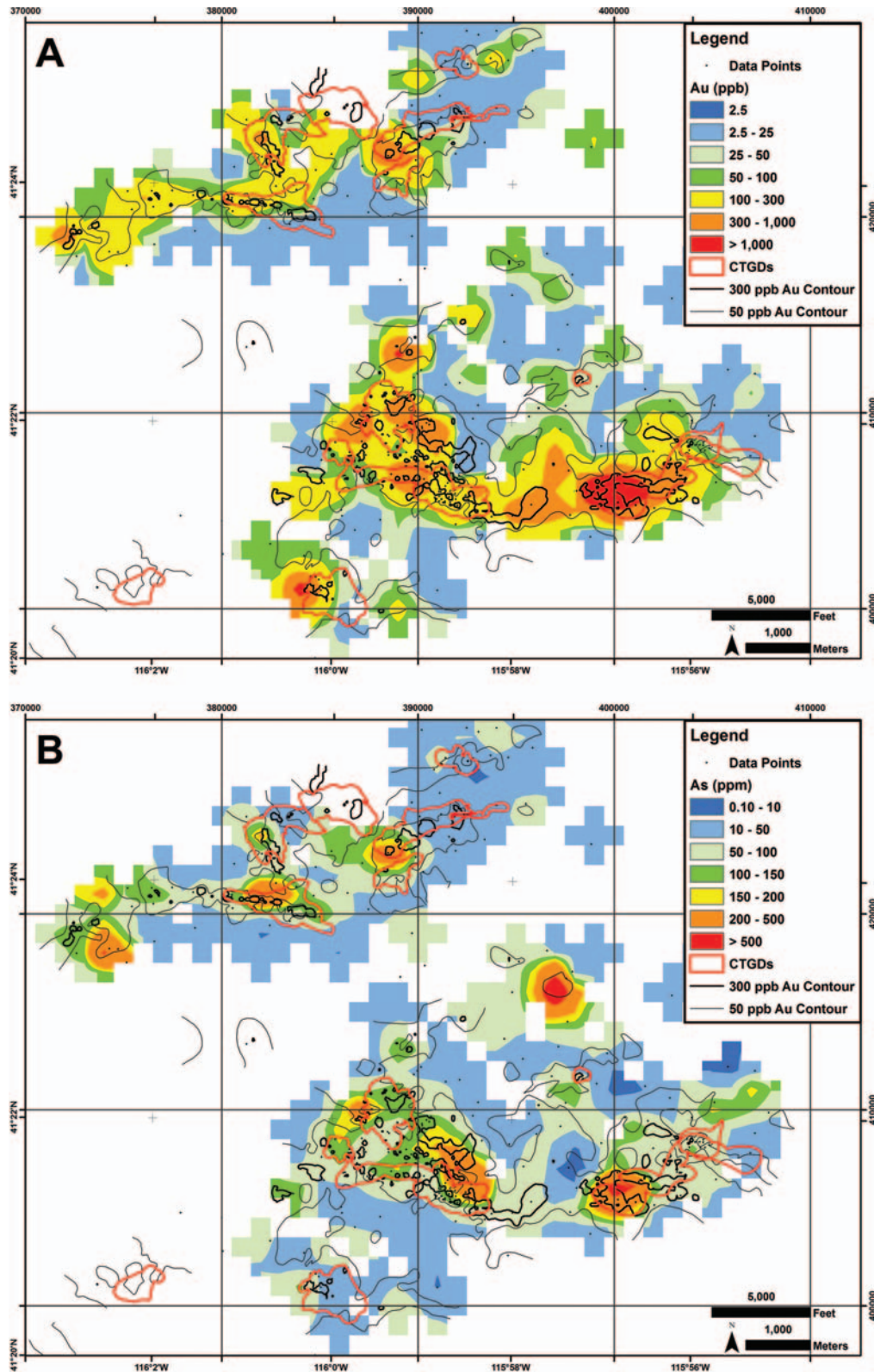
Figure 13. Maps of gridded values for A. Au and B. As, using only 247 samples (black dots), which were from holes that were re-logged as described by Patterson (2009). Same gridding procedure used as for the other gridded images, except a cell size of 1,000 feet, rather than 150 feet, was utilized. Also shows locations of the 300 ppb Au contours (thick black lines), the 50 ppb Au (thin back lines) contours, which are based on the entire data set, and outlines of the CTGDs (red lines). The legends are for the gridded values, not the actual values. Coordinates are longitude-latitude (tics, degrees-minutes, WGS84) and local Jerritt Canyon mine grid (grid lines, feet, NAD27 Nevada West State Plane modified by a false northing of -2,000,000 ft).
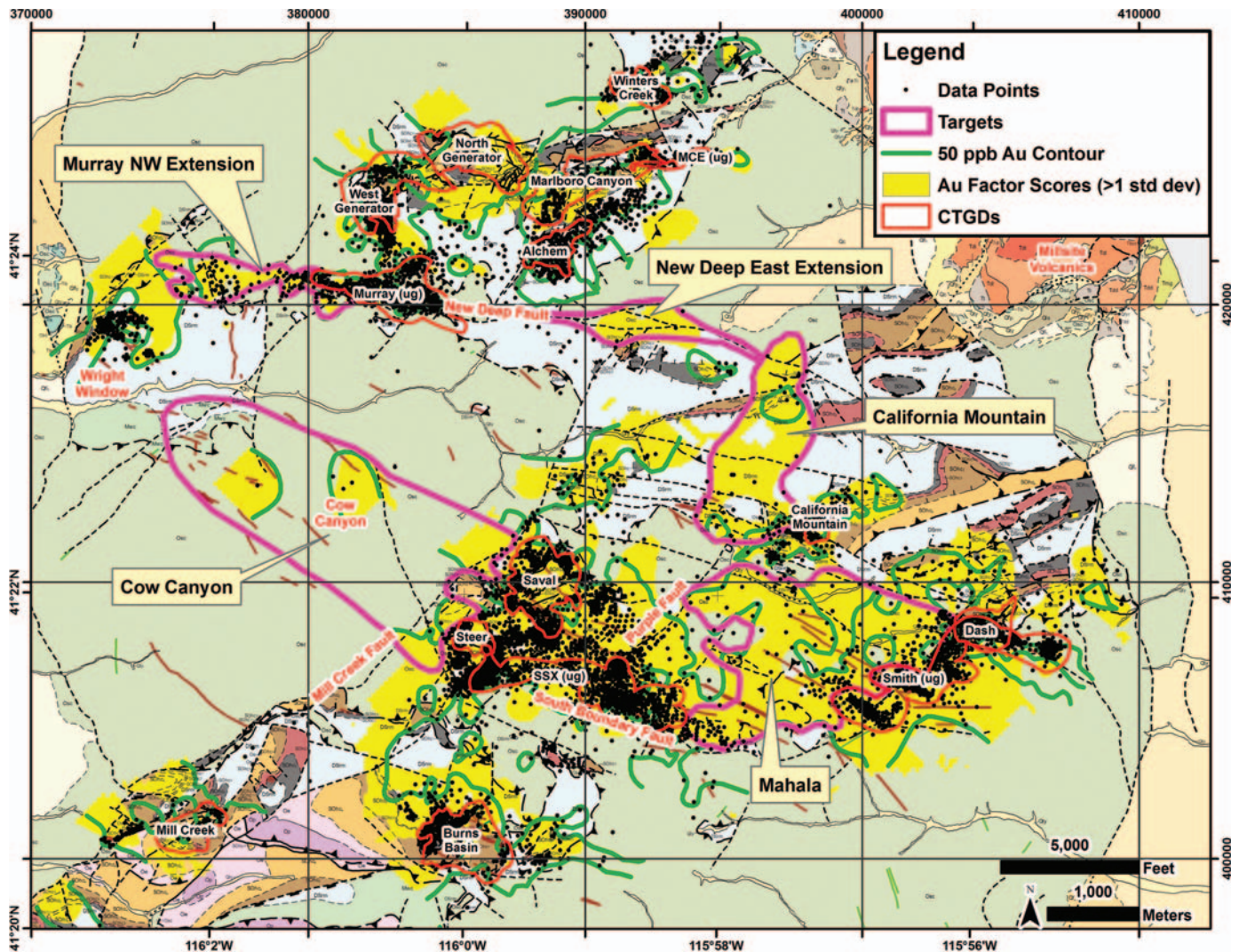
Figure 14. Geology map (same as Fig. 3) showing locations of targets (thick magenta outlines) discussed in text. Also shows location of CTGDs (red outlines), 50 ppb Au contours (thick green lines), high Au factor scores (1 standard deviation above the mean, yellow areas) and the surface projection of the Saval data points (black dots). Coordinates are longitude-latitude (tics, degrees-minutes, WGS84) and local Jerritt Canyon mine grid (grid lines, feet, NAD27 Nevada West State Plane modified by a false northing of -2,000,000 ft).

ments in the SSX/Smith area. It is located in the hanging wall of Mill Creek fault. Only five holes have been drilled, which indicate depths of 1,800 to 2,400 feet to the Saval.

REFERENCES

Abdi, H., 2003, Factor Rotations in Factor Analyses, *in* Lewis-Beck M., Bryman, A., and Futing, T. eds. Encyclopedia of Social Sciences Research Methods: Sage, Thousand Oaks, California, p. 1–8.

Arehart, G.B., and Donelick, R.A., 2006, Thermal and isotopic profiling of the Pipeline hydrothermal system: Application to exploration for Carlin-type gold deposits: Journal of Geochemical Exploration, p. 27–40.

Babcock Jr., R.C., Ballantyne, G.H., Phillips, C.H., 1995, Summary of the geology of the Bingham District, Utah: Arizona Geological Society Digest, v. 20, p. 316–335.

Bettles, K., 2002, Exploration and geology, 1962 to 2002, at the Goldstrike Property, Carlin Trend, Nevada *in* Thompson, T.B., Teal, L., and Meeuwig, R.O., eds., Gold Deposits of the Carlin Trend: Nevada Bureau of Mines and Geology, v. 111, p. 54–75.

Birak, D.J., and Hawkins, R.B., 1985, The Geology of the Enfield Bell Mine and the Jerritt Canyon District, Elko County, Nevada, *in* Tooker, E.W., ed., Geologic characteristics of sediment-and volcanic-hosted disseminated gold deposits-search for an occurrence model: U. S. Geological Survey Bulletin 1646, p. 95–106.

Bratland, C.T., 1991, Geology of the Winters Creek gold deposit, Independence Mountains, Elko County, Nevada, *in* Rains G.L., Lisle, R.E., Schafer, R.W., and Wilkinson, W.H., eds., Geology and Ore Deposits of the Great Basin: Geological Society of Nevada Symposium Proceedings, Reno, Nevada, p. 607–618.

Cail, T.L., and Cline, J.S., 2001, Alteration Associated with Gold Deposition at the Getchell Carlin-Type Gold Deposit, North-Central Nevada: Economic Geology, v. 96, p. 1343–1359.

Carr, J.R., 2002, Data Visualization in the Geosciences: Prentice Hall, Upper Saddle River, New Jersey, 267 p.

Cassinerio, M.D., and Muntean, J.L., 2010, Patterns of Lithology, Structure, Alteration and Trace Elements around High-grade Ore Zones at the Turquoise Ridge Gold Deposit, Getchell District, Nevada. (*GSN 2010 Symposium Volume, submitted*)

Chakurian, A.M., Arehart, G.G., Donelick, R.A., Zhang, X., and Reiners, P.W., 2003, Timing constraints of gold mineralization along the Carlin trend utilizing apatite fission-track, $^{40}Ar/^{39}Ar$, and apatite (U-Th)/He: Economic Geology, v. 98, p. 1159–1171.

Cline, J.S., Hofstra, A.H., Muntean, J L., Tosdal, R.M., and Hickey, K.A., 2005, Carlin-type gold deposits in Nevada: Critical geologic characteristics and viable Models, *in* Hedenquist, J. W., Thompson, J. F. H., Goldfarb, R. J., and Richards, J. P., eds., 100th Anniversary Volume: Society of Economic Geologists, Littleton, CO, p. 451–484.

Daly, W.E., Doe, T.C., and Loranger, R.J., 1991, Geology of the northern Independence Mountains, Elko County , Nevada, *in* Raines, G.L., Lisle, R.E., Schafer, R.W., and Wilkinson, W.H., eds., Geology and Ore Deposits of the Great Basin: Geological Society of Nevada Symposium Proceedings, Reno, Nevada, p. 583–602.

Dewitt, A.B., 1999, Alteration, geochemical dispersion, and ore controls at the SSX Mine, Jerritt Canyon District, Elko County, Nevada: Unpublished M.S. thesis, University of Nevada Reno, 95 p.

Dilles, P.A., Wright, W.A., Monteleone, S.E., Russell, K.D., Marlowe, K.E., Wood, R.A., and Margolis, J., 1996, The geology of the West Archimedes deposit: A new gold discovery in the Eureka mining district, Eureka County, Nevada, *in* Coyner, A.R., and Fahey, P.L., eds., Geology and Ore Deposits of the American Cordillera: Symposium Proceedings: Reno, Geological Society of Nevada, p. 159–171.

Eliason, R., and Wilton, D.T., 2005, Relation of gold mineralization to structure in the Jerritt Canyon mining district, Nevada, *in* Rhoden, H.N., Steininger, R.C., and Vikre, P.G., eds., Geological Society of Nevada Symposium 2005: Window to the World, Reno, Nevada, May 2005, p. 335–356.

Fulignati, P., and Sbrana A., 1998, Presence of native gold and tellurium in the active high-sulfidation hydrothermal system of the La Fossa volcano (Vulcano, Italy): Journal of Volcanology and Geothermal Research, v. 86, p. 187–198.

Heinrich, C.A., Günther, D., Audétat, A., Ulrich, T., and Frischknecht, R., 1999, Metal fractionation between magmatic brine and vapor, determined by microanalysis of fluid inclusions: Geology, v. 27, p. 755–758.

Heinrich, C.A., 2005, The physical and chemical evolution of low-salinity magmatic fluid at the porphyry to epithermal transition: a thermodynamic study: Mineralium Deposita, v. 39, p. 864–889.

Heitt, D.G., Dunbar, W.W. Thompson, T.B., and Jackson, R.G., 2003, Geology and Geochemistry of the Deep Star Gold Deposit, Carlin Trend, Nevada: Economic Geology, v. 98 p. 1107–1136.

Henry, C.D., 2008, Ash-flow tuffs and paleovalleys in northeastern Nevada: Implications for Eocene paleogeography and extension in the Sevier hinterland, northern Great Basin: Geosphere v. 4, p. 1–35.

Hofstra, A.H., 1994, Geology and genesis of the Carlin-type gold deposits in the Jerritt Canyon district, Nevada: Unpublished Ph.D. dissertation, Golden, Colorado School of Mines, 1287 p.

Hofstra, A.H., and Cline, J.S, 2000, Characteristics and models for Carlin-type gold deposits: in Reviews in Economic Geology, v.13, p. 163–220.

Hofstra, A.H., Leventhal, J.S., Northrop, H.R., Landis, G.P., Rye, R.O., Birak, D.J., and Dahl, A.R., 1991, Genesis of sediment-hosted disseminated gold deposits by fluid mixing and sulfidization: Chemical-reaction-path modeling of ore-depositional processes documented in the Jerritt Canyon District, Nevada: Geology, v. 19, p. 36–40.

Hofstra, A.H., Snee, L.W., Rye, R.O., Folger, H.W., Phinisey, J.D., Loranger, R.J., Dahl, A.R., Naeser, C.W., Stein, H.J., and Lewchuck, M., 1999, Age constraints on Jerritt Canyon and other Carlin-Type gold deposits in the western United States-relationship to mid-Tertiary extension and magmatism: Economic Geology, v. 94, p. 769–802.

Hutcherson, S.K., 2002, Geology, geochemistry and alteration of Zone 5 of the Murray Mine, Jerritt Canyon district, Elko County Nevada: Unpublished M.S. thesis, University of Nevada Reno, 114 p.

Jensen, E.P, and Barton, M.D., 2000, Gold Deposits Related to Alkaline Magmatism: Reviews in Economic Geology, v. 13, p. 279–314.

Jones, M., 2005, Jerritt Canyon District, Independence Mountains, Elko County Nevada, gold's at fault: Geological Society of Nevada Field Trip Guidebook 8 (Geological Society of Nevada Symposium 2005 Window to the World), p. 99–122.

Kerr, J.W., 1962, Paleozoic sequences and thrust slices of the Seetoya Mountains, Independence Range, Elko County, Nevada: Geological Society of America Bulletin, v. 73, p. 714.

Kesler, S.E., Ye, Z., Fortuna, J., and Riciputi, L.C., 2003, Epithermal Carlin transition: Evidence for magmatic input to Carlin-type deposits, *in* Eliopoulos, D. et al. eds., Mineral exploration and sustainable development: Rotterdam, Millpress, v. 1, p. 493–494.

Kuehn, C.A, and Rose, A.W., 1992, Geology and geochemistry of wall-rock alteration at the Carlin gold: Economic Geology, v. 87, p. 1697–1721.

Larocque, A.C.L., Stimac, J.A., Siebe, C., Greengrass, K., Chapman, R., and Mejia, S.R., 2008, Deposition of a high-sulfidation Au assemblage from a magmatic volatile phase, Volcán Popocatépetl, Mexico: Journal of Volcanology and Geothermal Research, v. 170, p. 51–60.

Longo, A.A., Cline, J.S., and Muntean, J.L., 2009, Using pyrite to track evolving fluid pathways and chemistry in Carlin-type deposits: *in* Ressel, M.W., Diverse Gold Deposits of the Osgood Mountains and Humboldt Range, North-Central, Nevada, Special Publication no. 49, p. 63–65.

MacKenzie, J.M., and Canil, D., 2008, Volatile heavy metal mobility in silicate liquids: Implications for volcanic degassing and eruption prediction: Earth and Planetary Science Letters, v. 269, p. 488–469.

McMillin, S.L., 2005, The discovery, production, and continued exploration of the SSX mine area, Jerritt Canyon, Nevada, *in* Rhoden, H.N., Steininger, R.C., and Vikre, P.G., eds., Geological Society of Nevada Symposium 2005: Window to the World, Reno, Nevada, May 2005, p. 453–468.

Muntean, J.L., and Henry, C.D., 2007, Preliminary geologic map of the north half of the Jerritt Canyon mining district, Elko County, Nevada: Nevada Bureau of Mines and Geology, Open File Report OF07-3.

Nevada Bureau of Mines and Geology, 2009, The Nevada Mineral Industry 2008: Special Publication MI-2008, p. 175.

Patterson, L.M., 2009, Hydrothermal footprint of Carlin-type gold deposits at the district scale: Jerritt Canyon mining district, Elko County, Nevada: Unpublished M.S. thesis, University of Nevada Reno, 240 p.

Peters, S.G., Armstrong, A.K., Harris, A.G., Oscarson, R.L., and Noble, P.J., 2003, Biostratigraphy and structure of Paleozoic host rocks and their relationship to Carlin-type gold deposits in the Jerritt Canyon mining district, Nevada: Economic Geology, v. 98, p. 317–337.

Phinisey, J.D., Hofstra, A.H., Snee, L.W., Roberts, T.T., Dahl, R.J., and Loranger, R.J., 1996, Evidence for multiple episodes of igneous and hydrothermal activity and constraints on the timing of gold mineralization, Jerritt Canyon district, Elko County, Nevada, *in* Coyner, A.R., and Fahey, R.L., eds., Geology and Ore Deposits of the American Cordillera: Geological Society of Nevada Symposium, Reno, 1995, Proceedings, v. 1, p. 15–39.

Rose, A.W., Hawkes, E.H., and Webb, J.S., 1980, Geochemistry in Mineral Exploration: Academic Press, 2nd edition, 657 p.

Stenger, D.P., Kesler, S.E., Peltonen, D.R and Tapper, C.J., 1998, Deposition of gold in Carlin-type deposits; the role of sulfidation and decarbonation at Twin Creeks, Nevada: Economic Geology vol. 93, p. 201–215.

Wells, J.D., Stoiser, L.R., and Elliot, J.E., 1969, Geology and geochemistry of the Cortez gold deposit, Nevada: Economic Geology, v. 64, p. 526–587.